AGU PUBLICATIONS

Journal of Advances in Modeling Earth Systems

RESEARCH ARTICLE
10.1002/2016MS000777

A computational study on the nature of meso-β scale vortex coalescence in a tropical atmosphere

David A. Schecter[1]

[1]NorthWest Research Associates, Boulder, Colorado, USA

Key Points:
- The mechanisms of meso-β scale vortex merger are diverse
- Diabatic processes in a cloud resolving model can either help or hinder merger
- Irrotational winds can be important in driving the system-centric influx of vorticity during merger in a dry adiabatic system

Correspondence to:
D. A. Schecter,
schecter@nwra.com

Citation:
Schecter, D. A. (2017), A computational study on the nature of meso-β scale vortex coalescence in a tropical atmosphere, *J. Adv. Model. Earth Syst.*, *9*, doi:10.1002/2016MS000777.

Received 15 AUG 2016
Accepted 26 APR 2017
Accepted article online 9 MAY 2017

Abstract Tropical weather systems commonly contain a variety of mesoscale vortices whose interactions may influence the timing of tropical cyclone formation. Previous computational studies have found that interactions ending in coalescence can either help or hinder development depending on the specific circumstances. Despite the potential importance of mesoscale vortex merger, complications introduced by baroclinic effects and diabatic processes have impeded progress toward elucidating its mechanics. The present study is an effort to advance current understanding by way of idealized numerical experiments with a cloud-permitting model. Direct comparisons are made between dry adiabatic and moist diabatic simulations of meso-β (20–200 km) scale vortex merger on a tropical oceanic f-plane. Consistent with a number of earlier studies, deep cumulus convection is found to accelerate the late stage of surface-concentrated vortex merger over a warm ocean. On the other hand, incorporating artificial radiation and cloud processes into the numerical model substantially hinders the merger of middle-tropospheric vortices over a moderately cooler ocean. Such hindering coincides with the partial suppression of shear-induced vortex misalignments whose amplifications and rotations appear to be essential to the dry adiabatic merger mechanism. The aforementioned dry merger mechanism is examined in detail. Irrotational winds linked to the horizontal divergence field are found to largely control the system-centric influx of absolute vorticity, in sharp contrast to ideal two-dimensional hydrodynamics. The consequences of lowering (raising) the sea-surface temperature under the moist surface-concentrated (middle-tropospheric) system are briefly addressed.

1. Introduction

Observational evidence suggests that tropical weather systems commonly contain a variety of mesoscale vortices originating from prior or active cloud processes [e.g., *Simpson et al*., 1997; *Reasor et al*., 2005; *Sippel et al*., 2006; *Houze et al*., 2009]. Theoretical considerations and computational studies (cited below) suggest that mesoscale vortex interactions have the potential to significantly affect the progression of tropical cyclone formation. Of particular relevance to this study are the interactions of meso-β (20–200 km) scale vortices ending in their coalescence. While there is a tendency in the literature to emphasize that such vortex merger can assist the development of a tropical cyclone [e.g., *Ritchie and Holland*, 1997; *Kieu and Zhang*, 2010], the process is variable and in certain scenarios might have the opposite effect [*Schecter*, 2016]. Despite its potentially profound importance in one way or another, vortex merger at the mesoscale remains minimally understood. The deficiencies in current understanding are largely attributable to complications arising from baroclinic effects and diabatic processes.

The basic purpose of this paper is to advance current knowledge of how diabatic processes change the nature of vortex merger. The primary methodology involves direct comparison between cloud-permitting and dry adiabatic numerical simulations. Specifically, this study examines the idealized problem of meso-β scale vortex merger on the tropical oceanic f-plane in the absence of environmental winds. Both midlevel and surface-concentrated merger events are investigated. The cloud-permitting simulations incorporate not only precipitating moist convection, but also artificial radiation and a basic parameterization of air-sea interaction.

To fully comprehend the impact of diabatic processes on vortex merger requires thorough understanding of the dry adiabatic dynamics. The binary systems considered herein are initially configured such that their baroclinic nature (vertical variation) is essential to the dry merger mechanism. The mechanism responsible

for the merger of baroclinic vortices is well-known to vary considerably with the specifics of the problem [e.g., *Verron and Valcke*, 1994; *Von Hardenberg et al*., 2000; *Schecter*, 2016]. The merger process of principal relevance to the present study is that described by *Schecter* [2016]. In the aforementioned scenario, the vortices become vertically misaligned as a result of their mutual shearing in the direction of orbital motion. The leading sections of the sheared vorticity cores then swing toward the center of the binary system and fuse, while the trailing sections of weaker intensity are expelled radially outward. *Schecter* [2016] theorizes and provides evidence that the preceding dynamics is simply the consequence of vortex misalignments having natural tendencies to rotate.

Adding moisture and radiation to the atmosphere clearly has the potential to modify or radically change the prevailing mechanism of mesoscale vortex coalescence. The confinement of air parcels to quasi-horizontal surfaces of constant dry entropy no longer applies. Diabatic warming/cooling creates volumes of air with positive or negative buoyancy that may ascend from the boundary layer to the tropopause, or descend to the surface and generate spreading cold pools. The attendant stretching/squashing, tilting, and advection of vorticity will to some extent alter the core structure of each mesoscale vortex in the binary system. Convective flow structures may also develop outside the vortex cores and influence merger therefrom.

Previous studies of vortex merger in numerical simulations of tropical cyclone formation have emphasized the potential for moist convection to accelerate if not fully cause the coalescence of mesoscale vorticity anomalies [e.g., *Hendricks et al*., 2004; *Tory et al*., 2006; *Fang and Zhang*, 2011]. It is commonly inferred that convergent flow related to moist convection helps bring the vortices together. As one might expect, similar conclusions on moist convection assisting merger can be found in earlier studies addressing the behavior of binary tropical cyclones [e.g., *Chang*, 1983; *Wang and Holland*, 1995]. Be that as it may, the generality of the principle that diabatic processes play a positive role in vortex coalescence has not gone unquestioned [*Falkovich et al*., 1995; *Khain et al*., 2000]. The principle just stated will be further challenged by several of the numerical experiments at hand.

This paper will first demonstrate that the importance of irrotational winds associated with the convergence and divergence of horizontal velocity is not restricted to diabatic systems. The irrotational winds will be found to play a leading role in the baroclinic merger mechanism that operates in the dry adiabatic simulations. It will be argued that such a leading role is consistent with the theory of merger by rotating misalignments proposed by *Schecter* [2016]. A by-product of the argument will be a new perspective on the nature of mesoscale vortex misalignment modes. Activation of artificial radiation and convective clouds will be found in several cases to hinder the aforementioned dry adiabatic merger mechanism and slow the progress of vortex coalescence. The potential for moist convection to substantially assist merger will not be seen to clearly take effect until relatively late times (if ever) in the simulations under consideration.

The remainder of this paper is organized as follows. Section 2 describes the setup of each numerical experiment and one of the more involved techniques used to analyze the data. Sections 3 and 4 present the results of selected midlevel and surface-concentrated vortex merger experiments. Section 3 also provides an addendum to the theory of vortex misalignment modes that is deemed necessary for understanding the experimental results. Section 5 discusses the findings of sections 3 and 4 and their sensitivities to the underlying sea-surface temperature. Section 6 reiterates the main conclusions. Appendices A and B provide technical details pertaining to the data analysis and the theory of vortex misalignment modes.

2. Methodology

2.1. Experimental Setup

All numerical experiments considered herein are conducted with version 18.3 of Cloud Model 1 [*Bryan and Fritsch*, 2002]. The model is configured on a doubly periodic f-plane with a marginally tropical setting of the Coriolis parameter given by $f = 5 \times 10^{-5}$ s^{-1}. The dynamical system is discretized on a stretched rectangular grid whose center coincides with the initial center of the binary system of interacting vortices to be studied. The horizontal grid spans approximately 3600 km in each orthogonal coordinate. The central square of the horizontal domain has increments of 1.67 km. The length of the central square is 574 km. At the four corners of the horizontal domain, the grid increments are 14.3 km. The vertical grid has 68 points and extends upward to $z = 30$ km, in which z denotes the height above sea level. The vertical grid spacing gradually increases from 50 to 540 to 750 m as z increases from 0 to 12 to 30 km.

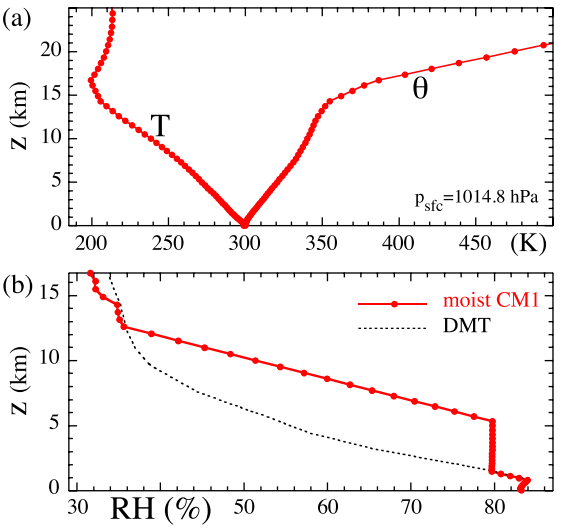

Figure 1. (a) Initial ambient temperature (T) and potential temperature (θ) profiles in the moist CM1 experiments. The dry experiments have equivalent stratification to within negligible error. The ambient surface pressure is printed on the lower-right corner of the graph. (b) The initial ambient relative humidity (RH) in the moist CM1 experiments compared to that of the Dunion moist tropical (DMT) sounding. The z axis terminates at the altitude (16.7 km) where the ambient water-vapor mixing ratio (q_v) in the moist CM1 experiments has a local minimum of 5.7×10^{-6}. The value of q_v grows to 4.1×10^{-5} at $z = 20.7$ km, and then decays with an e-folding rate of -0.24 km^{-1} as z goes further into the stratosphere.

Two classes of experiments are conducted: moist and dry. The moist experiments utilize the full energy conserving equation set available in CM1. Moisture is parameterized with a variant of the two-moment Morrison microphysics routine, having graupel as the large icy-hydrometeor category and a constant cloud droplet concentration of 100 cm^{-3} [*Morrison et al.*, 2005, 2009]. The effect of atmospheric radiation is crudely accounted for by nudging the potential temperature θ toward its ambient profile on a 12 h time scale or at a rate of ±2 K d^{-1} if the latter is slower [*Rotunno and Emanuel*, 1987]. Such thermal nudging is referred to in this paper as "artificial radiation." Subgrid turbulent transport is parameterized by an anisotropic Smagorinsky-type scheme, and dissipative heating is activated. Standard Rayleigh damping of upward propagating waves is imposed above $z_d = 25$ km. Surface fluxes are parameterized with bulk-aerodynamic formulas. Unless stated otherwise, the drag coefficient C_d is approximately based on *Fairall et al.* [2003] at low wind speeds and *Donelan et al.* [2004] at high wind speeds. In practice, C_d varies from 10^{-3} to 2.4×10^{-3}. The enthalpy exchange coefficient is set to 1.2×10^{-3} based on *Drennan et al.* [2007].

The primary dry experiments have no cloud microphysics, radiation, surface fluxes, dissipative heating, or stratospheric Rayleigh damping. The subgrid turbulence parameterization is similar to that in the moist experiments. Excluded elements other than cloud microphysics are restored for several important sensitivity tests.

Figure 1 shows the sounding used for the hydrostatically balanced ambient atmosphere in the moist CM1 experiments. The functional dependence of θ on z is equivalent to that in the dry experiments, and the vertical temperature (T) profile is negligibly different. Moreover, the ambient distributions of θ and T closely resemble their counterparts in the moist tropical sounding of *Dunion* [2011]. The relative humidity (RH) used for the moist experiments distinctly exceeds that of the Dunion sounding in the middle troposphere. Such enhancement of middle-tropospheric RH may better represent a weather system well into the priming process that facilitates tropical cyclogenesis [e.g., *Nolan*, 2007; *Smith and Montgomery*, 2012; *Davis and Ahijevych*, 2013]. The Convective Available Potential Energy (CAPE) and Convective Inhibition (CIN) of an undiluted surface parcel undergoing pseudoadiabatic ascent with liquid-only condensate in the moist environment are approximately 2.1×10^3 and 23 J kg^{-1}, respectively. The sea-surface temperature T_s has a constant value of 26.8 or 29.8 °C. Oceans with the lesser or greater surface temperature are concisely referred to as "cool" or "warm." In either case, T_s is sufficiently large to permit the convective development of a tropical cyclone over a meteorologically relevant time scale. Of greater relevance to the present study, a difference of 3 °C has the potential to substantially affect diabatic vortex coalescence.

The binary systems are initialized with two identical vortices whose maximum wind speeds exist either in the middle troposphere or near the surface. Specifically, each vortex is characterized by a cyclonic vertical vorticity distribution of the form

$$\zeta(r,z)=[\zeta_c\Theta(r_c-r)-\zeta_h\Theta(r_h-r)]\Upsilon(z), \tag{1}$$

in which r denotes radius from the center of the vortex, $\zeta_h=\zeta_c r_c^2/r_h^2$, and $\zeta_c=5\times10^{-4}$ s^{-1}. The Heaviside step function is defined such that $\Theta(\varpi)=1$ or 0 if the argument ϖ is greater than or less than 0, respectively. The radial profile of vorticity consists of a uniform positive core out to $r_c = 50$ km, surrounded by a negative

halo that brings the circulation to zero at $r_h = 500$ km. The preceding value for r_h ensures that the magnitude of halo vorticity associated with a single vortex is no greater than $0.07f$. The vertical structure function is given by

$$\Upsilon = \frac{e^{10/7}}{2\{\cosh[(z-z_*)/\delta h] + \cosh(10/7)\}}. \quad (2)$$

The constituent vortices of the midlevel systems are characterized by $z_*=5.5$ km and $\delta h=1.75$ km. Those of the surface-concentrated systems are characterized by $z_*=0.5$ km and $\delta h=2.47$ km. In each experiment, the vertical velocity field and the divergence of horizontal velocity are initially set to zero. The horizontal velocity, pressure, and virtual potential temperature (θ_v) fields are obtained from equations of nonlinear balance as explained in Appendix B1 of *Schecter* [2011]. The balance conditions are applied to the superposition of the two vorticity fields representing the mesoscale vortices, not to each vortex separately.

Figures 2a and 2b show cross sections of the initial velocity and θ_v fields in both the midlevel and surface-concentrated binary systems. The centers of each vortex are initially separated by 250 km in the horizontal plane. This particular separation distance is sufficiently small for merger to occur in both the midlevel and surface-concentrated binary systems. Moreover, it resides in an interval where baroclinic effects appear to have an essential role in the dry adiabatic merger mechanism [cf., *Schecter*, 2016].

Note that in the moist simulations, small-scale θ and vapor mixing ratio (q_v) perturbations are added to the initial conditions near the surface ($z \leq 1.25$ km) of each vortex core ($r \leq r_c$). The corresponding spatial fluctuations of θ and q_v have peak magnitudes of 1.5 K and 3 g/kg. Both perturbation fields are pseudo-randomly generated in one vortex and determined by reflectional symmetry about the system center in the other. Despite the perturbation-induced stimulation of cumulus activity at the outset, persistent deep convection requires several hours (for a surface-concentrated system at high T_s) to one and one-half days (for a midlevel system at low T_s) to materialize.

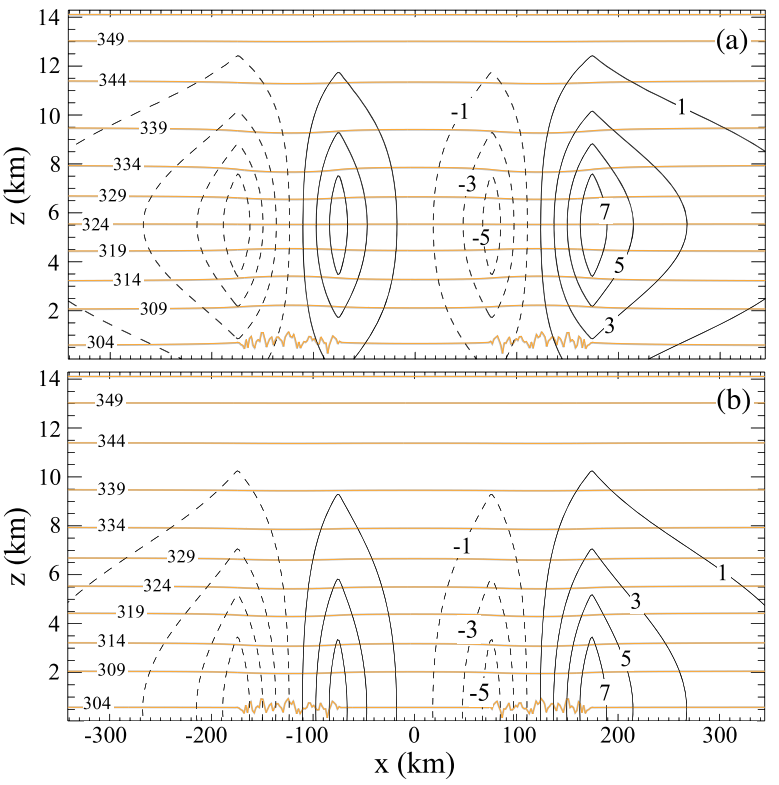

Figure 2. Vertical cross sections of the initial (a) midlevel and (b) surface-concentrated binary systems in the plane containing the central axes of both vortices. Black contours show the velocity field in the *y* direction, which is into the page. Solid/dashed contours representing positive/negative velocities are labeled in units of m s^{-1}. Orange-gray contours show the virtual potential temperature θ_v of the moist experiments, and are labeled in units of K.

There are several caveats of the experimental setup that should be explicitly mentioned. First, the initial conditions neglect the broad background vorticity distribution associated with the encompassing meso-α scale cyclone of a natural tropical weather system [e.g., *Dunkerton et al.*, 2009]. The experiments also exclude ambient vertical wind shear, and the meridional variation of the Coriolis parameter. The preceding factors are expected to modify both the adiabatic and diabatic pathways of meso-β scale vortex coalescence. It is envisioned that subsequent investigations will systematically address this issue, having results from the present study as a reference point. As in other basic modeling studies, artificial radiation is employed here primarily as a precaution against excessive atmospheric warming. Its influence on merger should not be viewed as wholly realistic. A more realistic parameterization of radiation might be expected to enhance aggregation of moist convection [*Bretherton et al.*, 2005] and accelerate the development of a rotational convective system into a tropical cyclone [*Davis*, 2015].

The forthcoming analysis in sections 3 and 4 will focus on the coalescence of midlevel vortices above a cool ocean or surface-concentrated vortices above a warm ocean. The aforementioned systems will adequately illustrate a variety of ways in which diabatic processes can affect merger. The consequences of raising (lowering) T_s in the moist midlevel (surface-concentrated) system will be addressed in section 5.

2.2. Coordinate Systems Used for Analysis

To prevent confusion hereafter, it is necessary to distinguish between vortex-centric and system-centric coordinate systems. In this paper, r and φ denote the radius and azimuth of a cylindrical coordinate system whose central axis coincides with that of an individual vortex in the binary system. By contrast, $\tilde{r}$ and $\tilde{\varphi}$ denote the radius and azimuth of a cylindrical coordinate system whose central axis coincides with that of the binary system as a whole.

The variables u, v, and w, respectively, denote the radial, azimuthal, and vertical velocity fields. In general, the coordinate system used to define u and v is readily gleaned from context. An overbar is used to denote an azimuthal average in either vortex-centric or system-centric analyses. An arbitrary field such as v may be written as follows: $v=\bar{v}+v'$, in which the prime denotes a perturbation from the azimuthal mean. Whereas both $\bar{v}$ and v' depend on radius, height (z) and time (t), only v' depends on the azimuth.

A vortex-centric coordinate system generally moves with the vortex. At each analysis time, the central axis is positioned at a selected rotational center inside the vortex. A rotational center is defined to be the origin of the polar coordinate system that maximizes the radial maximum of $\bar{v}$ at a particular height or in a particular vertical layer. In the latter case, $\bar{v}$ is taken to be a vertical average between the upper and lower boundaries of the layer. A system-centric coordinate system is generally held fixed over the applicable analysis period. Details of the method used to position its central axis slightly vary, and will be specified when the need arises.

2.3. Analysis of the Inner Spin-Up of a Binary System During Vortex Merger

The process of vortex merger generally coincides with the intensification of system-centric mean azimuthal velocity inward of the initial vortex positions. Comparing the sources of inner spin-up in the dry and moist experiments under consideration has led to some unexpected results and novel insights. A key element of the analysis is to decompose the source associated with the convergence of absolute vorticity into parts driven by irrotational and nondivergent winds. The specifics of this technique are described below.

2.3.1. The System-Centric Azimuthal Velocity Budget

The azimuthally averaged azimuthal velocity field in a system-centric coordinate system obeys the following equation of motion:

$$\frac{\partial \bar{v}}{\partial t} = -\overline{u\eta} - \overline{w}\overline{\frac{\partial v}{\partial z}} - \frac{C_p}{\tilde{r}}\overline{\theta'_\rho}\overline{\frac{\partial \Pi'}{\partial \tilde{\varphi}}} + \bar{F}_{\tilde{\varphi}}. \tag{3}$$

The first term on the right-hand side accounts for enhancement of the local circulation by the radial influx of absolute vorticity. The absolute vorticity is defined by $\eta \equiv \zeta + f$, in which $\zeta = [\partial(\tilde{r}v)/\partial\tilde{r} - \partial u/\partial\tilde{\varphi}]/\tilde{r}$. At a more fundamental level, the first and second terms on the right-hand side of equation (3) are proportional to the locally averaged radial and vertical advective tendencies of absolute angular momentum ($\mathcal{L} \equiv \tilde{r}v + f\tilde{r}^2/2$). Such is clear from the relations

$$\overline{u\eta} \equiv \frac{1}{\tilde{r}} \overline{u \frac{\partial \mathcal{L}}{\partial \tilde{r}}} \quad \text{and} \quad \overline{w \frac{\partial v}{\partial z}} \equiv \frac{1}{\tilde{r}} \overline{w \frac{\partial \mathcal{L}}{\partial z}}. \tag{4}$$

The third term is proportional to the pressure-gradient torque, written as the mean product of the isobaric specific heat of dry air (C_p), the density potential temperature perturbation (θ'_ρ), and the azimuthal gradient of the Exner function perturbation (Π'). The fourth term is proportional to the frictional torque, in which $F_{\tilde{\varphi}}$ is the azimuthal component of the acceleration vector associated with subgrid-scale turbulence in the model.

The azimuthal velocity tendency associated with the radial influx of absolute vorticity can be separated into distinct parts by way of a standard Helmholtz decomposition. The horizontal velocity field $\mathbf{u}$ is expanded as follows [cf., *Bishop*, 1996; *Renfrew et al*., 1997]:

$$\mathbf{u} \equiv \mathbf{u}_\chi + \mathbf{u}_\psi + \mathbf{u}_\vartheta. \tag{5}$$

By construction, $\nabla_h \times \mathbf{u}_\chi = 0$, $\nabla_h \cdot \mathbf{u}_\psi = 0$ and $\nabla_h \times \mathbf{u}_\vartheta = \nabla_h \cdot \mathbf{u}_\vartheta = 0$, in which ∇_h denotes the horizontal gradient operator. From the first two of the preceding relations, it follows that

$$\mathbf{u}_\chi \equiv \nabla_h \chi \quad \text{and} \quad \mathbf{u}_\psi \equiv \hat{z} \times \nabla_h \psi, \tag{6}$$

in which χ is a velocity potential and ψ is a stream function. Taking into consideration the combined irrotational and nondivergent nature of $\mathbf{u}_\vartheta$, it is also true that

$$\nabla_h^2 \chi = \sigma \quad \text{and} \quad \nabla_h^2 \psi = \zeta, \tag{7}$$

in which $\sigma \equiv \nabla_h \cdot \mathbf{u}$. For compact flows in unbounded domains or doubly periodic flows with zero mean velocity, standard solutions for, $\mathbf{u}_\chi$ and $\mathbf{u}_\psi$ coincide with $\mathbf{u}_\vartheta$ equal to zero. Confining the analysis to an arbitrary finite domain requires the judicious choice of a specific gauge which will determine $\mathbf{u}_\vartheta$. The method for calculating $\mathbf{u}_\chi$ and $\mathbf{u}_\psi$ for the present study is explained in Appendix A. Under this method, $\mathbf{u}_\vartheta$ is insignificantly small and will be neglected henceforth.

The foregoing Helmholtz decomposition (with $\mathbf{u}_\vartheta = 0$) yields

$$-\overline{u\eta} = -\overline{u_\chi \eta} - \overline{u_\psi \eta}. \tag{8}$$

In the ideal limit of inviscid nondivergent barotropic merger, $-\overline{u_\psi \eta}$ is the only nonzero contributor to system-centric spin-up inward of the binary vortices. A relatively large magnitude of $-\overline{u_\chi \eta}$ would therefore suggest a significant departure from an ideal two-dimensional merger mechanism. One might speculate that the departure is most pronounced when moist-convection is active. Forthcoming analysis will unexpectedly demonstrate that convergence of absolute vorticity by the irrotational flow ($\mathbf{u}_\chi$) can be equally if not more important during the merger of dry adiabatic vortices.

There will be one occasion in which we consider the azimuthal Fourier decomposition of $\overline{u\eta}$. The system-centric azimuthal Fourier expansion of a generic field variable has the form $g(\tilde{r}, \tilde{\varphi}, z, t) = \sum_{n=-\infty}^{\infty} g_n(\tilde{r}, z, t) e^{in\tilde{\varphi}}$. It is readily shown that

$$\overline{u\eta} = u_{\chi,0}\eta_0 + \sum_{n=1}^{\infty} 2\Re\left[u_{\chi,n}\eta_n^*\right] + \sum_{n=1}^{\infty} 2\Re\left[u_{\psi,n}\eta_n^*\right], \tag{9}$$

in which $\Re[\ldots]$ denotes the real part of the quantity in square brackets and the asterisk denotes the complex-conjugate. The first term on the right-hand side of equation (9) is the radial flux of absolute vorticity associated with the mean flow, which depends only on $u_\chi \eta$ owing to $u_{\psi,0} = 0$. The second and third terms on the right-hand side constitute the radial eddy-flux of absolute vorticity. In either component of the eddy-flux, η_n could be replaced with ζ_n owing to invariance of the Coriolis parameter on the f-plane.

3. The Merger of Middle Tropospheric Vortices

3.1. Dry Midlevel Merger

3.1.1. Experimental Importance of Irrotational Winds

Figure 3 illustrates the evolution of relative vorticity during dry adiabatic merger in a binary system initialized with midlevel vortices and configured with a free-slip bottom boundary condition. It is seen that

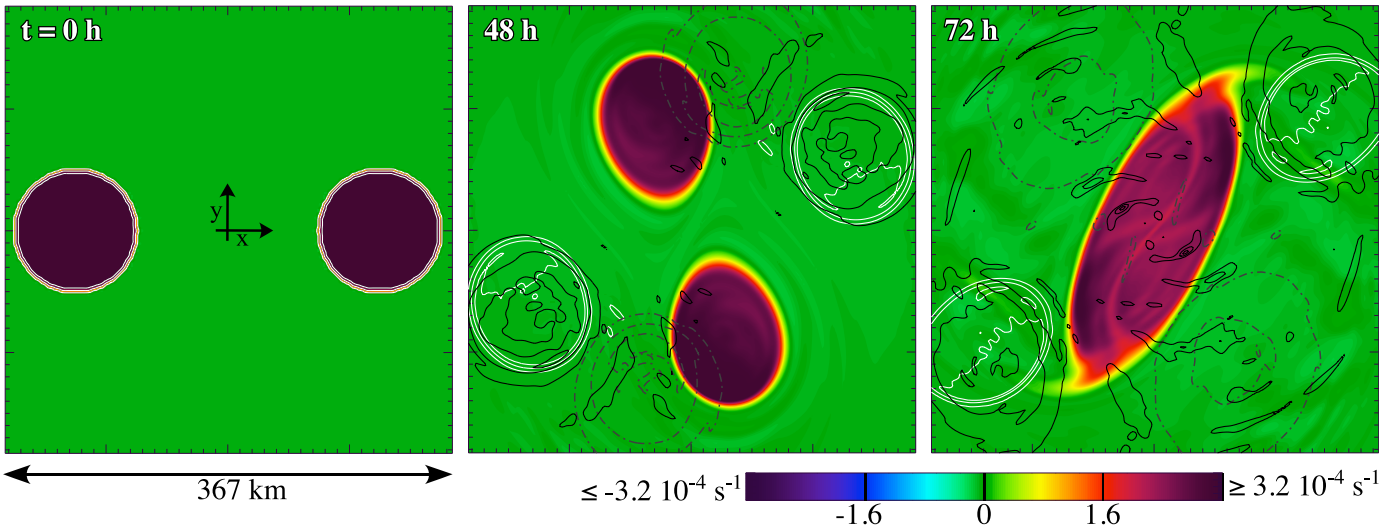

Figure 3. Evolution of relative vorticity ζ in the dry adiabatic midlevel binary vortex experiment (cf., Figure 2a). Colors show ζ at $z = 5.7$ km. Solid white and black contours respectively show ζ at $z = 0.08$ and 10.5 km, whereas the dash-dotted gray contours show ζ at $z = 2.8$ km. The first/second/third outermost contour of a nested set represents 0.1/0.5/0.9 times the initial maximum of ζ at the corresponding vertical level.

midlevel merger is attended by the expulsion of vorticity anomalies near the surface and in the upper troposphere. Such behavior is qualitatively consistent with merger caused by the natural rotations of misalignments generated in each vortex by exposure to the vertical shear-flow of its binary companion [*Schecter*, 2016, section 5 therein].

Figure 4 shows selected contributions to the change in the mean azimuthal velocity distribution ($\delta\bar{v}$) over the first 2 days of the 2.5–3 day merger process. The cylindrical coordinate system used for the present analysis is centered at the stationary midpoint between the two vortices. Contributions to $\delta\bar{v}$ associated with the pressure-torque and subgrid turbulent transport (friction) are not depicted owing to their relatively small magnitudes. Notably, the influx of absolute vorticity driven by the irrotational flow provides the largest contribution to midlevel spin-up inward of the initial orbital radius of the binary system, located at $\tilde{r} = 125$ km. Moreover, $-\overline{u_\chi \eta}$ largely accounts for the basic spatial pattern of $\delta\bar{v}$. The bottom row of Figure 4 portrays the azimuthal Fourier decomposition of $-\overline{u_\chi \eta}$. The symmetric ($n = 0$) component is seen to exceed but not dominate the sum of all asymmetric components. The $n = 1$ component is negligible, because the flow possesses approximate point-reflectional symmetry in the horizontal plane.

Figures 5a–5c show superimposed plots of the irrotational component of the radial velocity field (u_χ) and relative vorticity in the middle troposphere ($z = 5.3$ km) at several times during the 2 days under consideration. Figure 5a also shows the instantaneous streamlines of the irrotational vector velocity field $\mathbf{u}_\chi$. It is seen that the irrotational radial velocity field is characterized by strong negative peaks (corresponding to system-centric inward flow) within the midlevel vortex cores. Each cross-vortex flow pattern is connected to a convergence-divergence dipole straddling the core. The magnitude of u_χ at the center of each core is comparable to that required for its inward drift velocity.

A sensitivity experiment incorporating the surface drag parameterization of a moist simulation shows no significant quantitative change in the mechanics or timing of dry adiabatic midlevel merger. Another sensitivity experiment incorporating artificial radiation is unremarkable in showing midlevel merger coinciding with the expulsion of upper and lower tropospheric vorticity anomalies. On the other hand, core fusion is delayed until approximately 4 days have passed. The irrotational winds keep their leading role in driving the midlevel influx of absolute vorticity, but they no longer dominate the process. The spatial peak of $-\overline{u_\chi \eta}$ averaged over the first 2 days of merger is 1.3 times that of $-\overline{u_\psi \eta}$, compared to 2.4 in the original experiment. That artificial radiation should have a measurable effect on merger seems very reasonable. Artificial radiation simultaneously cools the upper warm-core and warms the lower cold-core of a midlevel cyclone, inducing a secondary circulation with middle-tropospheric outflow. Experimentally, imposing artificial radiation on a dry midlevel vortex similar to those used in the merger experiments causes the maximum wind

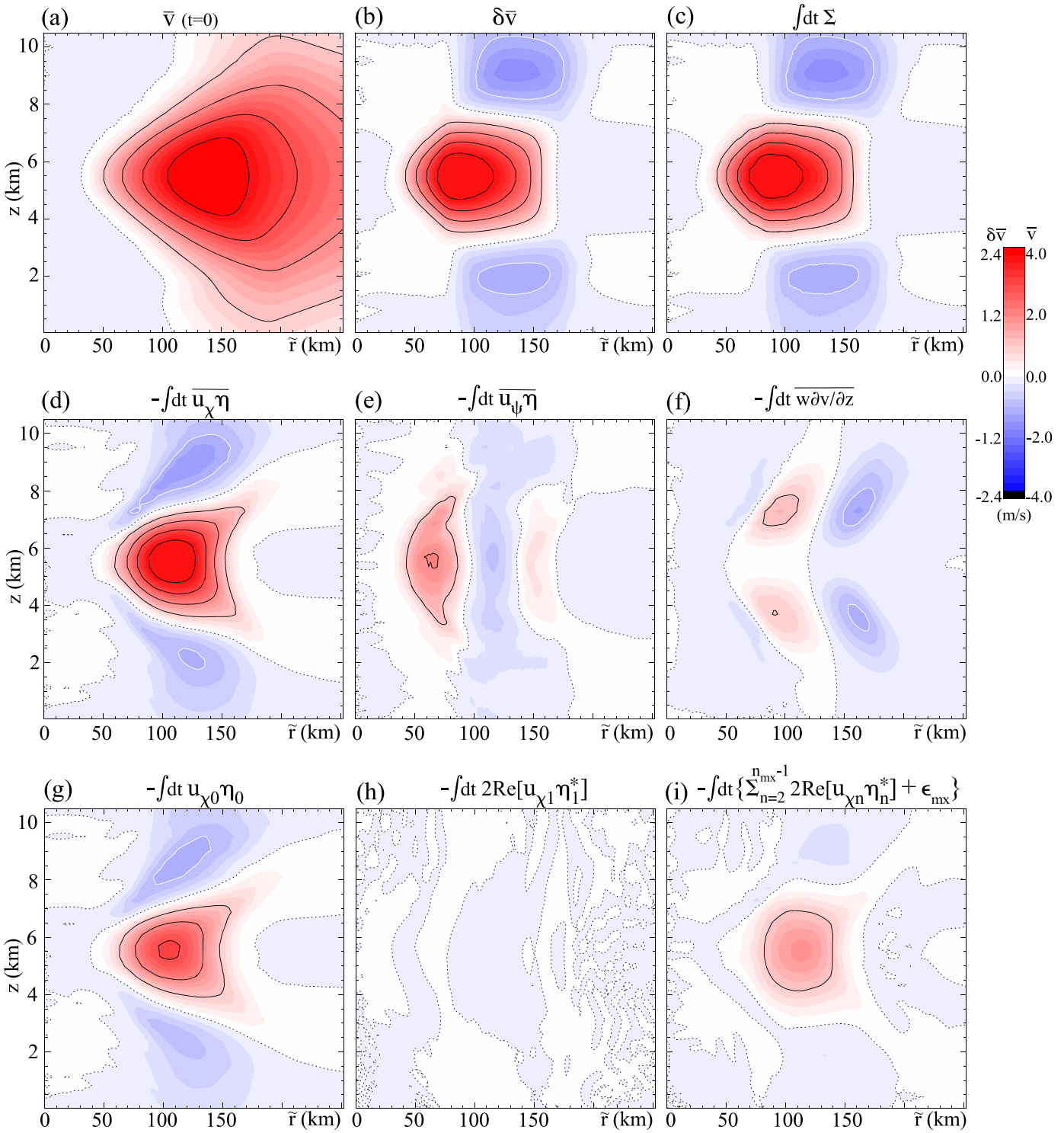

Figure 4. Azimuthal velocity budget in a system-centric coordinate system during the first 2 days of merger in the dry adiabatic midlevel binary vortex experiment. (a) The initial azimuthally averaged azimuthal velocity field $\bar{v}$ shown for reference. The contour interval is 1 m s^{-1}. (b) Change in $\bar{v}$ (denoted $\delta\bar{v}$) during the first 2 days of the experiment. The contour interval is 0.6 m s^{-1}. (c)–(f) Two day time integrals of (c) the sum of all tendency terms (Σ) on the right-hand side of equation (3), (d) the radial influx of absolute vorticity driven by the irrotational winds, (e) the radial influx of absolute vorticity driven by the nondivergent winds, and (f) the vertical advective tendency. (g)–(i) Contributions from wave numbers (g) 0, (h) 1, and (i) 2–n_{mx} to the time integral of $-\overline{u_\chi \eta}$, with ϵ_{mx} in the title of (i) representing a minuscule addition from the Nyquist wave number (n_{mx}=512). The contours in Figures 4c–4i are as in Figure 4b. In all plots, solid-black/solid-white/dotted contours represent positive/negative/zero velocities.

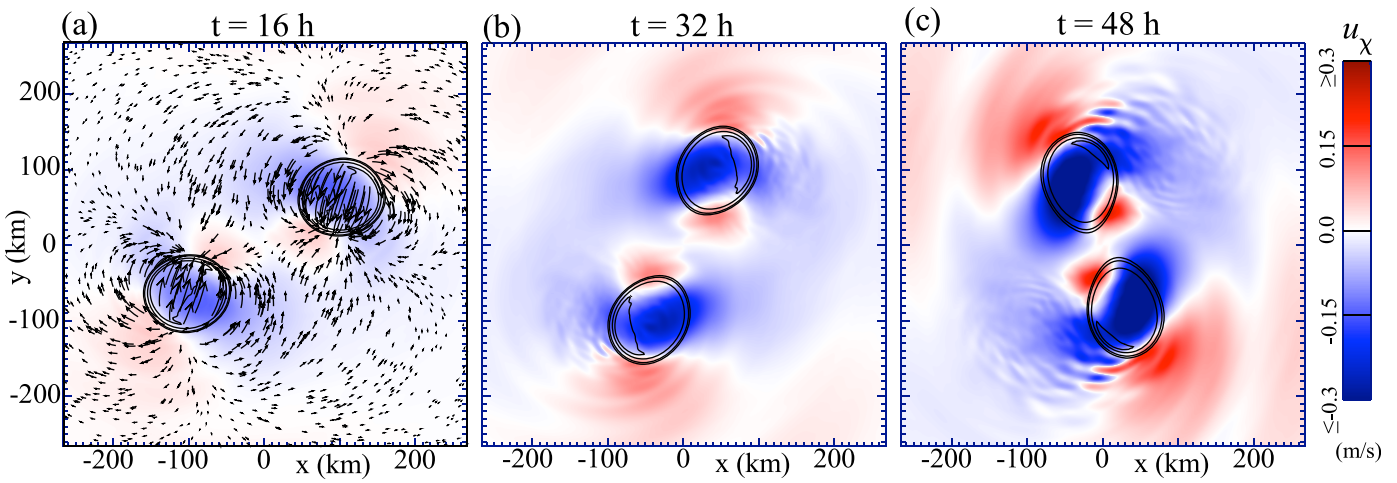

Figure 5. Snapshots of the middle-tropospheric irrotational winds and vortex cores in the dry adiabatic midlevel binary vortex experiment. (a) Streamlines and radial component of the irrotational velocity field $\mathbf{u}_\chi$, along with contours of relative vorticity at $z = 5.3$ km and $t = 16$ h. Streamline segments are tipped with arrows pointing in the direction of $\mathbf{u}_\chi$ and are proportional in length to $|\mathbf{u}_\chi|$. The color scale for the radial component of $\mathbf{u}_\chi$ is shown to the far right. The first/second/third/fourth outermost relative vorticity contour corresponds to 0.025/0.1/0.5/0.9 times the instantaneous maximum of ζ. (b, c) Same as Figure 5a but without streamlines and at later times indicated on the top of each plot.

speed to decay by 18% over two days, compared to 3% without thermal forcing. The difference between middle-tropospheric ($z = 5.7$ km) and surface $\bar{v}$ at the vortex interaction radius (250 km) decays by 53%. Further discussion of how artificial radiation might hinder midlevel merger is deferred until section 3.2.1.

3.1.2. Theoretical Role of Irrotational Winds

It is appropriate to ask if the prominent role of the irrotational winds in the dry merger mechanism is consistent with a process driven by the natural rotations of misaligned vortices [cf., *Schecter*, 2016]. The following examines whether the irrotational winds should have a dominant role in controlling the rotation of a misalignment in the mesoscale parameter regime of the numerical experiments.

Consider the relatively simple scenario of an isolated vortex on the f-plane whose basic state is barotropic and devoid of secondary circulation [cf., Appendix B]. Suppose that a small-amplitude misalignment mode with a vertical wavelength of *2H* (Figure 6a) is introduced at $t = 0$. Assuming that the mode is neutral, the misalignment will rotate at a constant angular frequency ω about the central axis of the vortex without growth or decay. In principle, the fluid parcels that carry the central potential vorticity of the unperturbed vortex at each vertical level—here called the PV centroids—are rigidly locked into the modal rotation

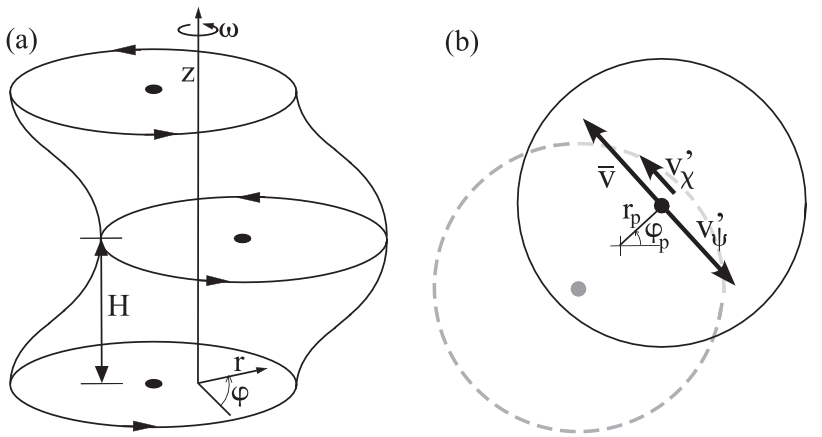

Figure 6. Depiction of a dry adiabatic misalignment mode in the basic parameter regime of the midlevel binary vortex experiments. (a) Illustration of the *z*-dependent displacements of PV centroids (dots) and horizontal circulations characteristic of a misalignment mode. (b) Decomposition of the azimuthal velocity at the midlevel PV centroid undergoing uniform circular motion about the central axis of the vortex. The nondivergent component of the perturbation (v'_ψ) nearly balances the completely nondivergent velocity of the basic state ($\bar{v}$), allowing the irrotational velocity perturbation (v'_χ) to play an important role in the rotation of the mode. The black and gray dots (circles) represent PV centroids (PV contours) at $z = H$ and $z = 0$, respectively.

[Appendix B2]. In other words, all of the displaced PV centroids will undergo uniform circular motion about the central axis with angular velocity ω.

To elaborate, let $(u', v') = a[U(r), V(r)]e^{i(\varphi-\omega t)}\cos(\pi z/H) + c.c.$ represent the horizontal velocity perturbation associated with the misalignment mode, and (r_p, φ_p, z_p) denote the cylindrical coordinates of a PV centroid. According to the theoretical arguments of Appendix B2,

$$r_p = 2\left|\frac{aU_0\cos(\pi z_{pi}/H)}{\omega-\bar{\Omega}_0}\right| \tag{10}$$

and $d\varphi_p/dt = \omega$ to lowest order in the mode amplitude $|a|$. In the preceding equation for r_p, U_0 and $\bar{\Omega}_0$ are U and $\bar{\Omega} \equiv \bar{v}/r$ evaluated in the limit $r \to 0$, whereas z_{pi} is the initial value of z_p.

Insight into the issue at hand can be obtained by decomposing the angular velocity of the PV centroid as follows:

$$\begin{aligned}\frac{d\varphi_p}{dt} &= \bar{\Omega}(r_p) + \frac{v'_\chi(r_p, \varphi_p, z_p, t)}{r_p} + \frac{v'_\psi(r_p, \varphi_p, z_p, t)}{r_p} \\ &\equiv \bar{\Omega}_0 \quad + \quad \omega_\chi \quad + \quad \omega_\psi,\end{aligned} \tag{11}$$

in which v'_χ (v'_ψ) is the irrotational (nondivergent) component of the azimuthal velocity perturbation, and ω_χ (ω_ψ) is the corresponding contribution to the angular velocity. Since the error is second order in $|a|$, it is justifiable to have made the substitution $\bar{\Omega}(r_p) \to \bar{\Omega}_0$ in the bottom line. As explained in Appendix B3, it can be shown that

$$\omega_{\chi/\psi} = \frac{|V_{0,\chi/\psi}|}{|V_0|}\cos\left(\varphi_{v0,\chi/\psi} - \varphi_{v0}\right)(\omega-\bar{\Omega}_0), \tag{12}$$

in which $V_0 = V(0)$, $V_{0,\chi/\psi}$ is the irrotational/nondivergent component of V_0, φ_{v0} is the argument of V_0, and $\varphi_{v0,\chi/\psi}$ is the argument of $V_{0,\chi/\psi}$.

For illustrative purposes, it is reasonable to consider a smoothed Rankine vortex (equation (B9)) with maximum wind speed $\bar{v}_m = 5.3$ m s^{-1} and core radius $r_c = 50$ km in an environment with $f = 5\times10^{-5}$ s^{-1} and a Brunt-Väisälä frequency N equal to 0.011 s^{-1}. The preceding parameters roughly correspond to those of the midlevel vortex experiments, with $\bar{v}_m$ equaling the average radial maximum of $\bar{v}$ between $z = 0$ and 11 km. An appropriate setting for the vertical half-wavelength of the misalignment is $H = 5.5$ km. The Rossby and rotational Froude numbers are, respectively, $\mathrm{Ro} \equiv 2\bar{v}_m/fr_c = 4.3$ and $\mathrm{Fr} \equiv \pi\bar{v}_m/NH = 0.28$. For the remainder of this subsection, frequencies will be normalized to $\bar{\Omega}_0$.

A numerical solution to the pertinent eigenmode problem (described in Appendix B1) shows that the misalignment mode of interest has an angular phase velocity of $\omega = 0.060$. The same solution shows that the irrotational and nondivergent components of the angular velocity perturbation at the centroid position are $\omega_\chi = 0.043$ and $\omega_\psi = -0.984$. Note that within round-off error, the preceding values are consistent with the relation $\omega = \bar{\Omega}_0 + \omega_\chi + \omega_\psi$, in which $\bar{\Omega}_0 = 1$. Although $|\omega_\chi| \ll |\bar{\Omega}_0|$ and $|\omega_\psi|$, the magnitude of ω_χ is considerably larger than that of the total nondivergent component of the centroid's angular velocity, $\bar{\Omega}_0 + \omega_\psi = 0.016$. Figure 6b illustrates the foregoing state of affairs. The vortex-centric angular velocity of a PV centroid is linked to its system-centric radial motion in the binary vortex experiments. It stands to reason that the prominent role of system-centric u_χ in these experiments does not overtly contradict the merger theory based on rotating misalignments in *Schecter* [2016].

3.2. Moist Midlevel Merger Over A Relatively Cool Ocean

3.2.1. Episode 1

Figure 7 illustrates the evolution of relative vorticity in the lower and middle troposphere during the merger of midlevel vortices in a moist system over a cool ocean ($T_s = 26.8$°C) with artificial radiation and a standard parameterization of sea-surface fluxes. Before the first depicted snapshot, subvortex-scale convection begins generating concentrated relative vorticity anomalies through mechanisms such as the tilting and stretching of vortex tubes [e.g., *Montgomery et al.*, 2006]. Vigorous deep convection starts in earnest approximately 1.4 days into the simulation. Once invigorated, cumulus updrafts and attendant downdrafts engender markedly complex changes to the horizontal flows in the relatively weak surface and uppermost

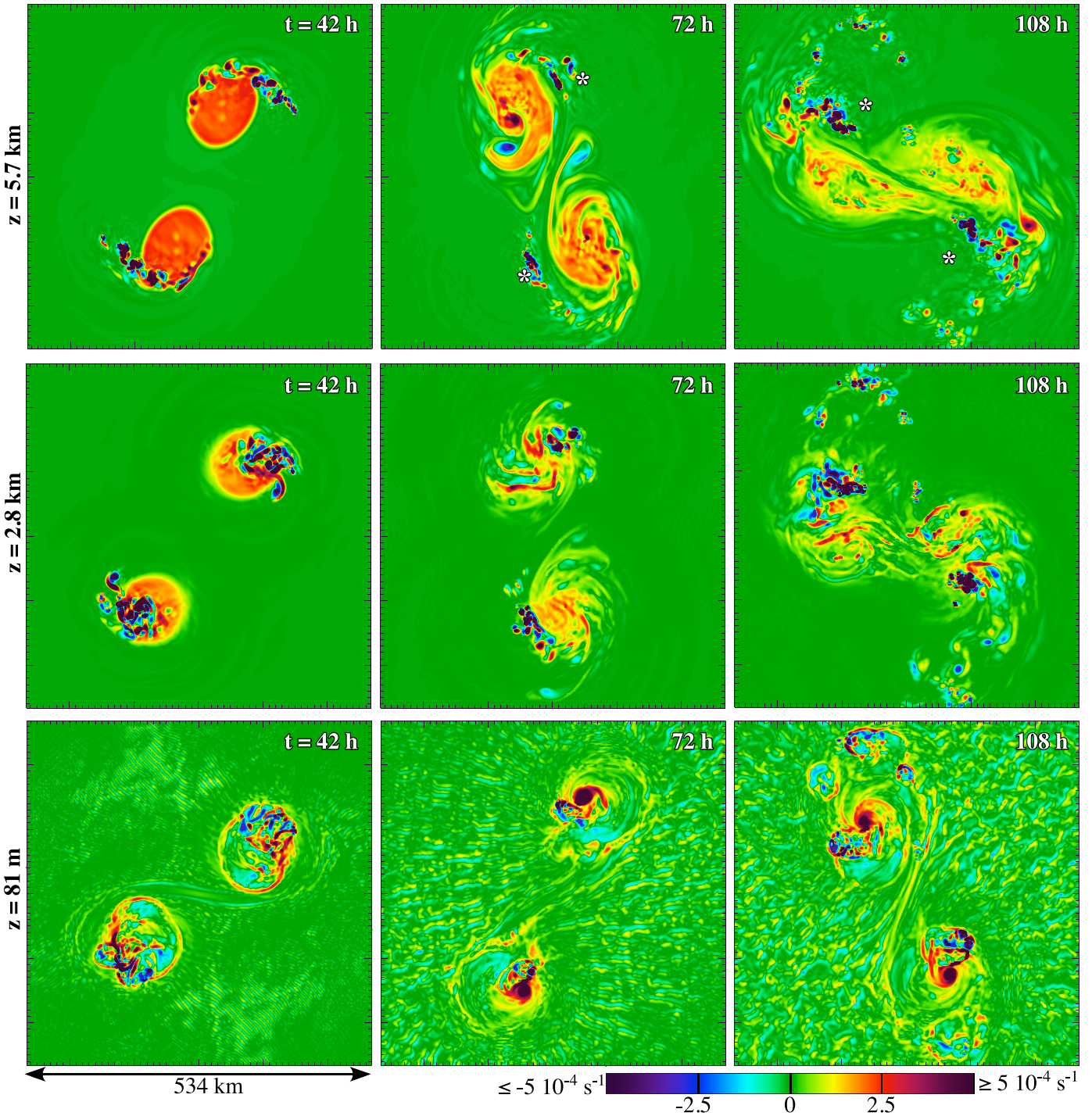

Figure 7. Evolution of relative vorticity in the moist midlevel system over a cool ocean at (top) $z = 5.7$ km, (middle) $z = 2.8$ km, and (bottom) $z = 81$ m. The time corresponding to each snapshot is shown in the top-right corner of each plot, whereas the altitude is printed to the left of each row. The white stars in two of the top plots show the surface vortex positions.

sections of the vortex cores. The near-surface flow in the bottom row of Figure 7 is characterized by contracted cyclonic eddies, filaments, pools of anticyclonic relative vorticity, and significant irrotational winds (not shown). The alterations to ζ caused by moist convection in between the vertical extremities of the vortex cores are substantial but arguably less dramatic, especially in the middle-tropospheric layer where the initial winds are maximal. Vortex circulations measured by $2\pi r\bar{v}$ at $r = 100$ km decay by 15% at $z = 5.7$ km but grow by 56% in the 1 km boundary layer over 3.5 days.

The binary vortices complete midlevel merger during the fifth day of the simulation, while their surface sections remain far apart. The near 5 day merger period is almost twice that found in the dry adiabatic experiment with or without surface drag. In this sense, the present result appears to starkly differ from a number of earlier studies finding that moist convection accelerates the merger of convective vorticity anomalies in developing systems [e.g., *Hendricks et al.*, 2004; *Fang and Zhang*, 2011] or of well-formed tropical cyclones [e.g., *Wang and Holland*, 1995]. However, as noted earlier, incorporating artificial radiation alone into the dry model can hinder midlevel merger. The time of core fusion in the aforementioned dry diabatic experiment is moderately less than that seen in the moist diabatic experiment at hand. Therefore, while moist convection is not fully responsible for the slowdown of midlevel merger, one may safely conclude that it fails to expedite the process.

Further understanding of the slowdown of midlevel merger is obtained by further comparison of the moist and dry simulations. Figure 8a shows the trajectories of lower-tropospheric and midlevel rotational centers in each vortex during the first 66 h of the moist experiment (Figure 7) and the first 62 h of the primary dry adiabatic experiment (Figure 3). The horizontal position of each rotational center is determined by the method explained in section 2.2. The trajectories in the moist experiment are seen to differ appreciably from their dry adiabatic counterparts in both spread and distance covered.

Of particular note, each vortex in the moist experiment exhibits slower development of vertical misalignment. Figure 8b explicitly demonstrates the hampered growth of misalignment, quantified by

$$\text{tilt} \equiv |\mathbf{x}_m - \mathbf{x}_l|, \tag{13}$$

in which $\mathbf{x}_m$ ($\mathbf{x}_l$) denotes the horizontal position vector of the rotational center at the middle tropospheric altitude z_m (lower-tropospheric altitude z_l) within a specific vortex. There are two plotted measures of tilt, both averaged between the two vortices. In general, z_m is taken to be 5.7 km. The results are qualitatively similar whether $z_l = 0.17$ or 2.9 km.

Enhanced resistance to misalignment under vertical shear when cloudy air and diabatically forced secondary circulations are present within a vortex is consistent with expectations stemming from earlier theoretical and computational studies on the subject [e.g., *Wang and Holland*, 1996; *Reasor et al.*, 2004; *Zhang and Kieu*, 2006; *Reasor and Montgomery*, 2015; *Schecter*, 2015]. A distinct feature of the present scenario is that diabatic forcing associated with artificial radiation alone appears to have a significant role in limiting tilt. The moist system becomes appreciably more effective at limiting tilt than a dry system with artificial radiation (purple curves in Figure 8b) only after 2 days have passed. Elucidating precisely how buoyancy modifications and secondary circulations induced by artificial radiation might help each vortex resist vertical shear

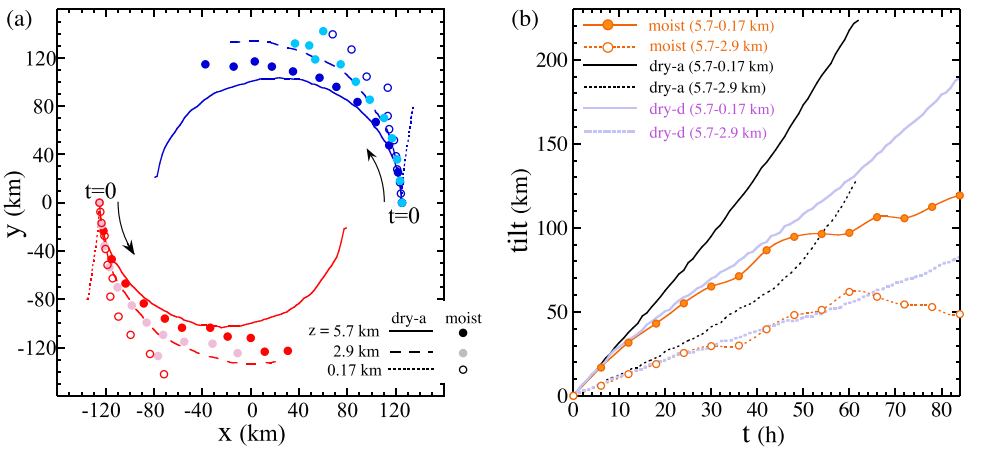

Figure 8. (a) Trajectories of the rotational centers of both vortices (red and blue) in the moist midlevel system over a cool ocean (circles) and its dry adiabatic counterpart (lines). Different symbol-shades and line-styles show the trajectories at different altitudes, as indicated in the legend. The black arrows point in the direction of time. The end-time of the dry/moist data is $t = 62/t = 66$ h. Data from the moist system are plotted in 6 h intervals. (b) Time series of two vortex-averaged "tilt" measurements in the moist (orange), dry adiabatic (black), and dry diabatic (purple) experiments. Solid (dotted) lines represent tilts defined with respect to the circulation centers at $z_m = 5.7$ km and $z_l = 0.17$ (2.9) km.

would be involved and is best left to a separate study. Both the symmetric and asymmetric components of the thermal forcing are presumably relevant. The significance of the former was briefly addressed in the last paragraph of section 3.1.1. The significance of the latter seems likely, not least because the applied potential temperature relaxation rate (2 d^{-1}) is nonnegligible compared to the estimated intrinsic frequency of a dry adiabatic misalignment mode ($\omega - \bar{\Omega} \sim 10$ d^{-1}) in the parameter regime of interest (section 3.1.2). Note that enhanced internal opposition to misalignment under fixed vertical wind shear is not the sole theoretical cause of diminished tilt. A decline of baroclinicity in each vortex of a diabatic binary system—an effect mentioned earlier —may also weaken their mutual shearing. In principle, the reduction of misalignments resulting from either artificial radiation or convective clouds within the vortices will hinder the midlevel merger mechanism of *Schecter* [2016].

Analysis of the system-centric $\bar{v}$-budget provides another interesting perspective on the distinction between diabatic and adiabatic dynamics. Figures 9a–9c show selected elements of the aforementioned $\bar{v}$-budget between hours 54 and 66 of the moist experiment, during which deep convection is accentuated on the outer side of each vortex. The polar coordinate center used for the present analysis (and that of section 3.2.2) is the initial midpoint between the two vortices. At the start of the analysis period, the midlevel

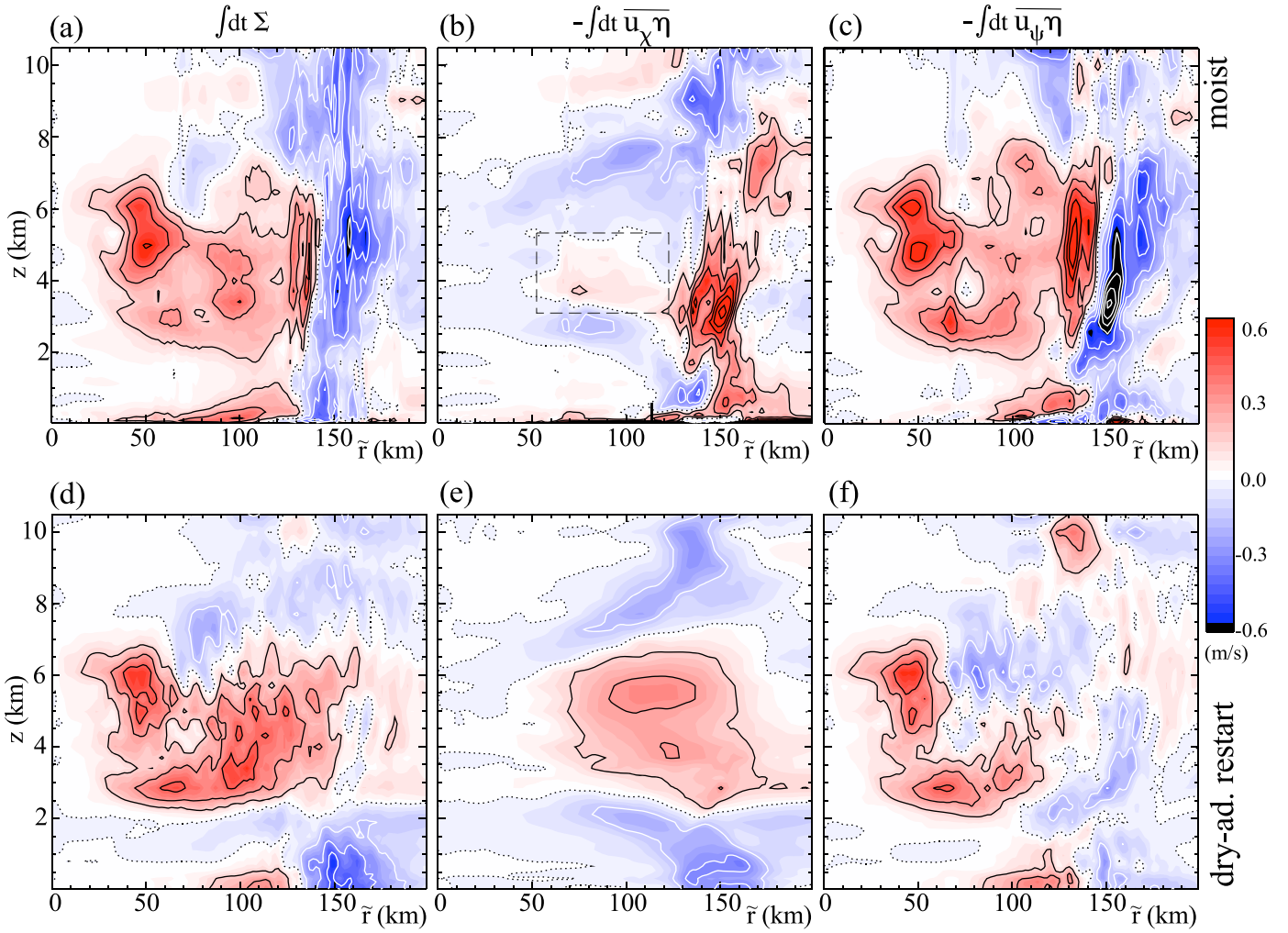

Figure 9. (a)–(c) Analysis of the system-centric change in $\bar{v}$ between hours 54 and 66 of the moist midlevel binary vortex experiment at low T_s. (a) The sum of all tendency terms (Σ) on the right-hand side of equation (3) integrated over the analysis period, shown for reference. (b, c) Similar time integrals of the tendencies associated with the radial influx of η driven by (b) the irrotational winds and (c) the nondivergent winds. (d)–(f) Same as Figures 9a–9c but for the first 12 h of a dry adiabatic restart initiated at the beginning of the moist analysis period. In each plot, the contours are styled after those in Figure 4 and are spaced 0.15 m s^{-1} apart. In Figure 9b, the black-dashed rectangle is the averaging area used in the text for quantitatively comparing $-\overline{u_\chi \eta}$ in the moist and dry simulations; the extended tick mark on the bottom axis indicates where the midlevel rotational centers of the vortices are located at $t = 54$ h.

vortex separation distance is comparable to that found by the end of day 1 in the primary dry adiabatic merger experiment. Over the next 12 h, the rotational centers of the binary vortices modestly converge (diverge) in the 1.5 km layer immediately below (above) the middle tropospheric altitude of 4.8 km. In contrast to the first 2 days of the primary dry adiabatic simulation (Figure 4), the positive contribution of nondivergent winds to the radial influx of absolute vorticity exceeds the weak and partly negative contribution from the irrotational winds in the inner middle-tropospheric region of the binary system. In the outer part of the binary system, the two components of $-\overline{u\eta}$ are heavily influenced by local cumulus forcing; their values are comparable in magnitude, but opposite in sign where peaked.

Figures 9d–9f show selected elements of the system-centric $\bar{v}$-budget over the first 12 h of a dry adiabatic restart that excludes surface drag. The restart is essentially initialized with the nondivergent winds of the moist experiment at $t = 54$ h, and with all other fields determined by nonlinear balance [cf., *Schecter*, 2011, Appendix B1]. The initial velocity field near the newly free-slip surface (below 320 m) is made invariant with respect to z. A few aspects of the dry adiabatic $\bar{v}$-budget resemble the moist results, but the differences are deemed to be of greater interest. Clearly, the outer imprints of localized cumulus forcing have been largely eliminated. Furthermore, $-\overline{u_\chi \eta}$ has a greater positive distribution inward of $\check{r} = 130$ km in the middle troposphere. The extent to which the latter is connected to the elimination of artificial radiation as opposed to moisture can be assessed by reintroducing the associated thermal relaxation scheme into the dry restart. The main result is an overall reduction of $-\overline{u_\chi \eta}$ in the middle troposphere, but not enough to account for what is seen in the moist experiment. In the dry/moist system having artificial radiation, the average of $-\overline{u_\chi \eta}$ within the dashed-black rectangle in Figure 9b is 58%/16% of that found in the dry adiabatic system. It is proposed that the persistent inhibition of vortex misalignments due to both cloud processes and artificial radiation contributes to the inner weakening of $-\overline{u_\chi \eta}$. The preceding inference is based on the theoretical connection between misalignment and $-\overline{u_\chi \eta}$ addressed in section 3.1.2. In support of the inference, it has been verified that the positive change of vortex-averaged tilt measured between $z = 5.7$ and 0.17 km in the moist experiment (dry restart with artificial radiation) is only 26% (82%) of that found in the dry adiabatic restart over the 12 h analysis period.

Additional insight on the failure of moist convection to accelerate midlevel merger is attained by examining the spatial distribution of strong precipitating updrafts. Figure 10a shows the accumulated rainfall and midlevel vortex trajectories over the first 114 h of the moist simulation. Figure 10b is a typical plot of accumulated rainfall over a 2 h time period superimposed on concurrent outlines of the midlevel and near-surface vorticity cores. Figures 10c and 10d depict the corresponding lower and upper tropospheric vertical velocity fields in one of the two misaligned vortices. The much weaker and dissimilar vertical velocity fields in the dry adiabatic restart are shown for reference (Figures 10e and 10f) [cf., *Jones*, 1995]. It is seen that deep moist convection lies in between the midlevel and surface centers of rotation. One might readily imagine that convergence into the area of the convective cluster contributes to hindering misalignment and the dependent dry merger mechanism. The pronounced cumulus activity further acts to redirect the irrotational flow away from the center of the binary system over a broad region of the midlevel vorticity core. Figure 11 illustrates the redirection induced by the combination of convection and artificial radiation by comparing $\mathbf{u}_\chi$ in the moist simulation to its counterpart in the dry adiabatic restart. Returning to the broader pattern of rainfall revealed over time (Figure 10a), it is seen that dense precipitation and deep convection (by association) primarily stay outward of the midlevel rotational centers of each vortex prior to coalescence. The absence of deep convection inward of the vortices precludes a conceivably efficient diabatic merger mechanism, in which centralized cumulus activity would create substantial mean inflow below the upper troposphere.

Although diabatic forcing diminishes the role of the original dry adiabatic merger mechanism, the attendant flow modifications do not work entirely against vortex coalescence. One previously undiscussed but notable feature of the moist system that appears to facilitate eventual merger is the gradual expansion of the midlevel vorticity cores. On average between the two vortices, the midlevel (vortex-centric) radius of maximum $\bar{v}$ steadily grows at a rate of 0.16 km h^{-1} prior to the onset of rapid fusion. A similar expansion is seen in the dry system with artificial radiation, but not in the dry adiabatic experiment. Even without additional factors nudging the vortices together, the slow but steady broadening of midlevel vorticity cores over a 100 h time scale would bring their radii substantially closer to the critical value required to trigger a 2-D rapid fusion event.

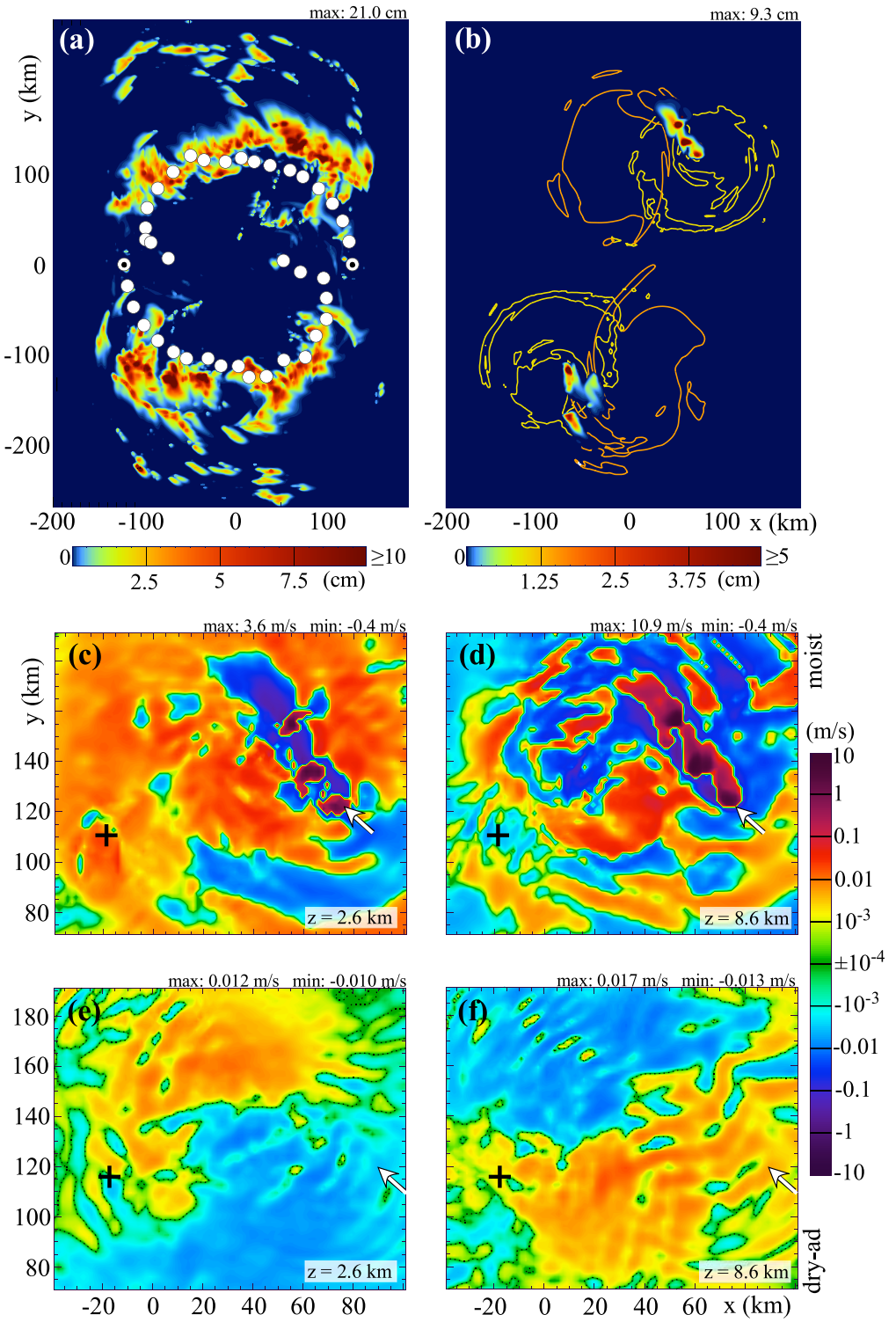

Figure 10. Convection in the midlevel binary system over a cool ocean. (a) Accumulated rainfall over the first 114 h of the moist simulation. White circles show the counter-clockwise trajectories of the rotational centers of each vortex at $z=z_m=5.7$ km. The rotational centers are plotted every 6 h starting from the circles with central black dots. (b) Accumulated rainfall between hours 59 and 61 of the moist simulation superimposed on the 5×10^{-5} s^{-1} contours of ζ averaged over the same time period, at $z=z_m$ (orange) and 0.15 km (yellow). (c) Vertical velocity (w) in one of the two vortices, averaged between hours 59 and 61 of the moist simulation at $z=2.6$ km. The central shade of green is for all grid points with $|w|\leq10^{-4}$ m s^{-1}. The black + and the tip of the white arrow mark the rotational centers of the local vortex at $z=z_m$ and 0.17 km, respectively. (d) As in Figure 10c but for w at $z=8.6$ km. (e, f) As in Figures 10c and 10d but for the dry adiabatic restart in the bottom row of Figure 9; the dotted contour shows where $w=0$.

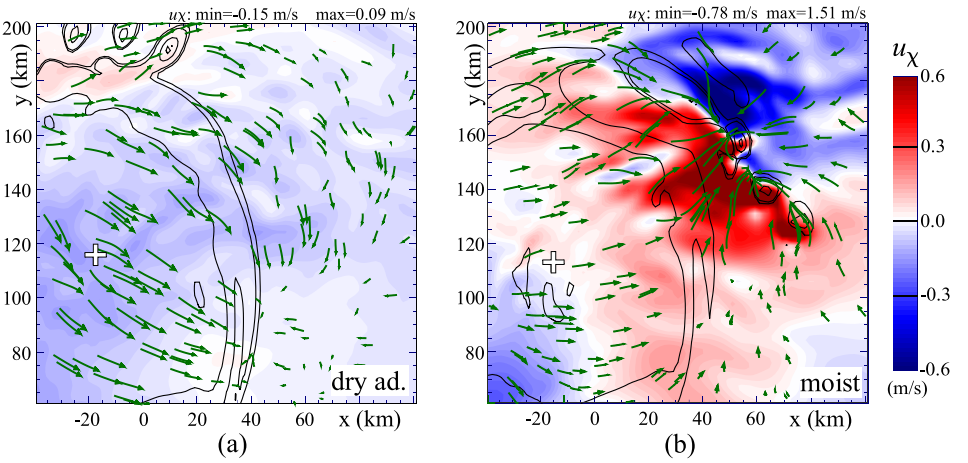

Figure 11. Diabatic redirection of irrotational flow in the vicinity of a midlevel vorticity core. (a) Streamlines (green arrows) of the irrotational velocity field $\mathbf{u}_\chi$ superimposed on a plot of its system-centric radial component u_χ (red and blue) and contours of relative vorticity ζ (black) in the dry adiabatic, hour-54 restart of the moist midlevel merger experiment over a cool ocean. The plotted fields are averaged over the interval $59 \leq t \leq 61$ h and shown at $z = 5.7$ km. The first/second/third/fourth outermost relative vorticity contour corresponds to 0.025/0.1/0.5/0.9 times the maximum of ζ in the depicted region of the flow. (b) As in Figure 11a but for the aforementioned moist experiment. The streamline segments are proportional to the local irrotational velocity in each plot, but the scaling differs between Figures 11a and 11b. Bear in mind that the actual flow has a larger contribution from the nondivergent circulation of the local vortex centered (at $z = 5.7$ km) on the white +. The coordinates are as in Figure 10.

3.2.2. Episode 2

After coalescence of the initial midlevel vortices into a broader elliptical cyclone, convective processes in the moist system produce a second generation of midlevel vortices. Two of the new vortices stand out on opposite ends of the major axis of the ellipse. Figure 12a illustrates their subsequent coalescence at $z = 4.6$ km. Figure 13 (middle row) shows the primary contributions to the change in system-centric $\bar{v}$ over the first 12 h of the merger process. In the middle troposphere, the accelerations are largely controlled by the influx of absolute vorticity driven by the nondivergent velocity field. The influx of η driven by the irrotational velocity field is evidently more important to the spin-up of the system-scale surface cyclone.

During its first 12 h, the second midlevel merger process strays little from that of a dry adiabatic restart with surface-drag eliminated, irrotational winds removed, and nonlinear balance imposed at the beginning. The similarity is evident upon examination of the system-centric $\bar{v}$-tendency terms above the boundary layer of the dry system (Figures 13g–13i). As in the moist experiment, the influx of η driven by u_ψ dominates. There is no indication that the irrotational winds play an important role in the coalescence of the midlevel vortices, in sharp contrast to the dry adiabatic version of the first merger process (Figure 4).

The leading role of u_ψ in driving the middle-tropospheric influx of η suggests that the second episode of midlevel merger might closely resemble an ideal 2-D process. It is straightforward to test the preceding speculation.

Figure 12b illustrates how merger progresses in a nondivergent 2-D model initialized with the middle tropospheric ($z = 4.6$ km) relative vorticity distribution at $t = 150$ h. The nondivergent 2-D model employs a standard vortex-in-cell (VIC) algorithm in a doubly periodic domain with both positive and negative vorticity parcels [cf., *Schecter et al.*, 1999]. The grid used by the VIC algorithm covers an area equivalent to that spanned by the CM1 grid, with increments of 1.75 km. It is seen that the ideal 2-D merger process is only moderately slower than its 3-D moist diabatic counterpart (Figure 12a) over a 20 h time frame in which the vorticity cores converge to a point of imminent unification. Although cumulus convection perturbs the moist system over time, the 2-D model seems to largely capture the vortex-scale dynamics.

Because of its apparent relevance, the nature of the 2-D merger mechanism merits further consideration. Notably, the 2-D merger mechanism requires the interaction between the vortex cores and the inhomogeneous background vorticity distribution. By replacing relative vorticity less than 2×10^{-4} s^{-1} in magnitude with a weak uniform background distribution at the start, merger does not occur for at least 2 days (Figure 12c). The preceding result seems reasonable in view of the known potential for enhanced mutual attraction of vortex cores possessing extended vorticity skirts [*DeMaria and Chan*, 1984; *Ritchie and Holland*, 1993],

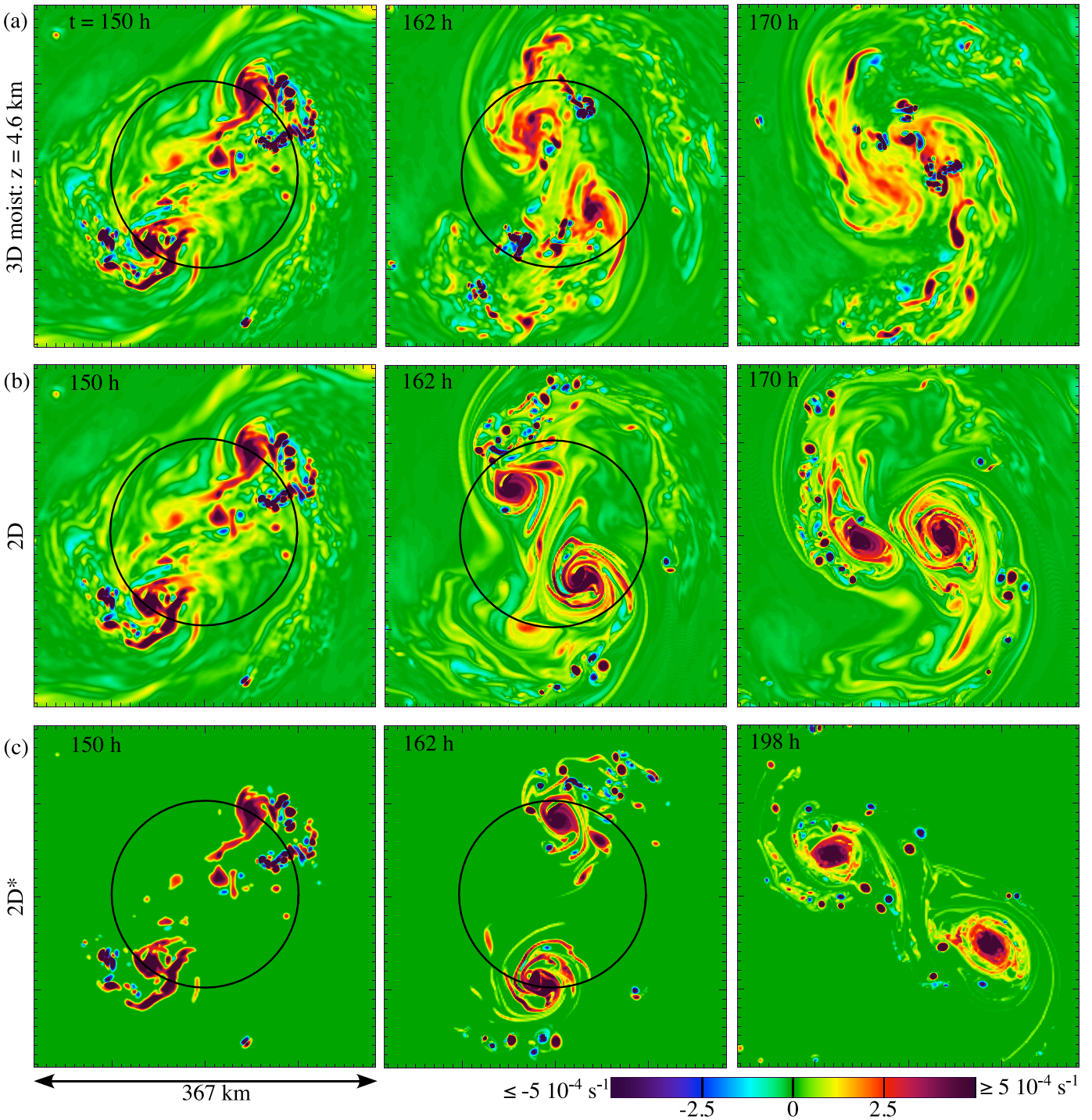

Figure 12. (a) Evolution of middle tropospheric relative vorticity during episode 2 of moist midlevel merger over a cool ocean. (b) Same as (a) but for a 2D nondivergent simulation initialized with the relative vorticity in (a) at $t = 150$ h. (c) Same as (b) but with relative vorticity less than $2 \times 10^{-4}\,s^{-1}$ in magnitude replaced with a weak uniform background distribution at the start. The snapshot time measured from the beginning of the moist experiment is printed on the upper-left corner of each plot. The black circles in the left and middle columns are for reference.

and the known potential for the "anomalous merger" of compact vortices interacting with large-scale vorticity or potential vorticity gradients [*Carnevale et al.*, 1991; *Soga et al.*, 2003].

Owing to the general interest in how vortex coalescence affects tropical cyclogenesis, it is worth noting that neither the first nor second episodes of midlevel merger appear to stimulate a major amplification of the

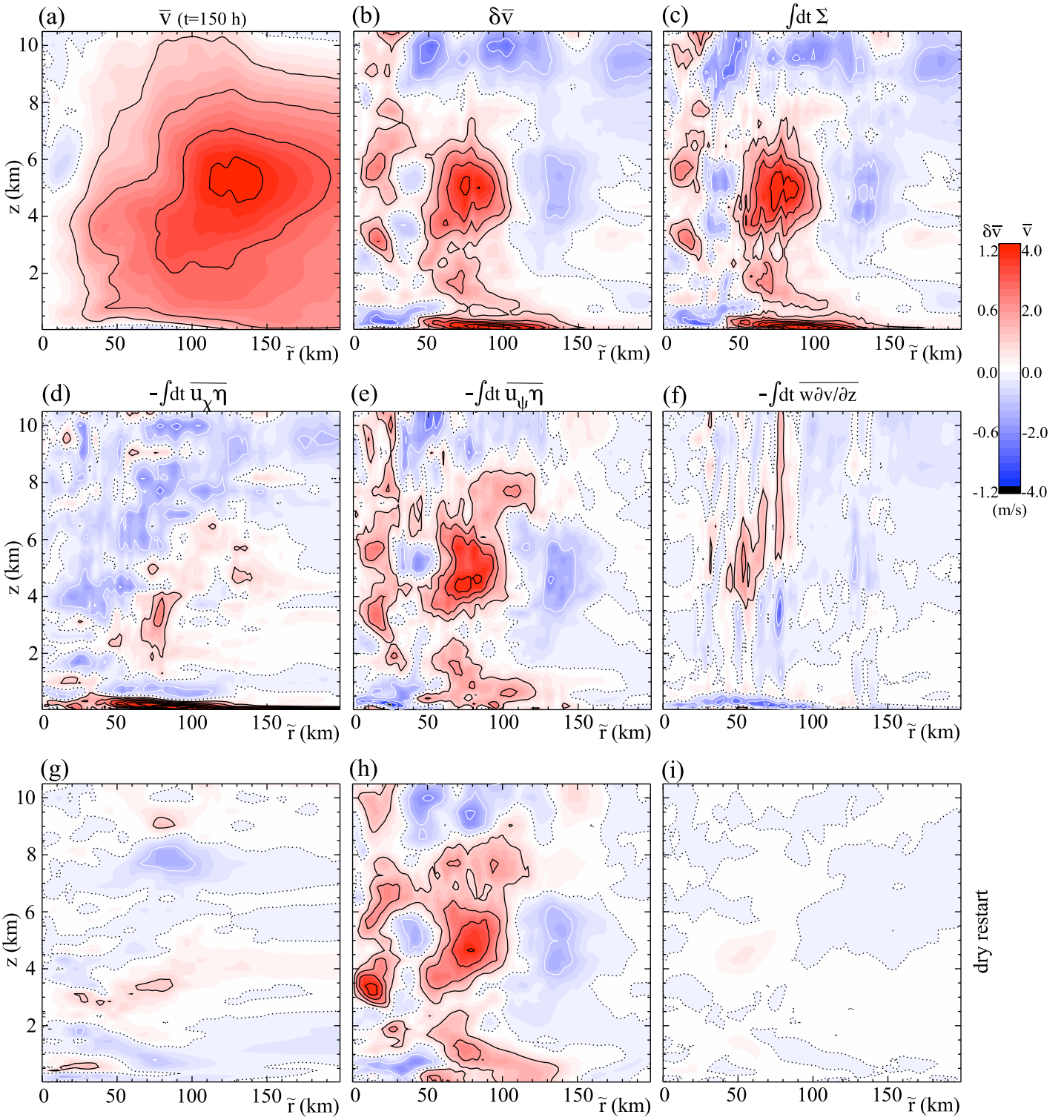

Figure 13. (a)–(f) As in Figures 4a–4f, but for hours 150–162 of the moist midlevel binary vortex experiment at low T_s. (g)–(i) As in Figures 13d–13f but for the initial 12 h of a dry adiabatic restart begun 150 h into the aforementioned moist experiment. Contours in Figure 13a are in intervals of 1 m s^{-1}, whereas contours in Figures 13b–13i are in intervals of 0.3 m s^{-1}.

surface winds. Moreover, the system fails to generate a tropical cyclone before the end of the 12 day simulation. Whether the system is in a binary or monopole state, vortex-centric values of $\bar{v}$ in the boundary layer never exceed 4–5 m s^{-1}. The author speculates that development is inhibited not only by a relatively cool

ocean and weak initial surface flow, but also by the initial binary interaction [*Schecter*, 2016]. A supplemental experiment has shown that an isolated midlevel vortex (equal to one of the binary vortices) under the same environmental conditions and governed by the same equations begins rapid intensification into a strong tropical cyclone within 4–5 days.

4. Lower Tropospheric Merger Over A Relatively Warm Ocean

The following examines the coalescence of surface-concentrated vortices in a moist-convective system over a warm ocean ($T_s = 29.8°C$) with artificial radiation and a standard parameterization of sea-surface fluxes. Results are discussed in comparison to the behavior of a dry adiabatic system. Sensitivity tests are conducted where necessary to help clarify key findings.

4.1. Basic Descriptions of the Dry Adiabatic and Moist Experiments

The dry adiabatic interaction of surface-concentrated vortices on a free-slip boundary begins with their mutual shearing. Subsequently, the lower vorticity anomalies move inward and the upper anomalies move outward. The dynamics is qualitatively similar to that seen in a dry midlevel system, but with the bottom half of each vortex erased and the midsection shifted to the surface. Analysis of the system-centric $\bar{v}$-budget verifies that the irrotational winds are largely responsible for the low-level influx of absolute vorticity during the merger process. Adding surface friction without moisture leads to gradual spin-down near the base of each vortex, and moderate slowdown of merger.

Figure 14a demonstrates that moist diabatic vortices also begin their mutual approach on a frictional surface at a discernibly slower rate than dry adiabatic vortices that are free of drag. Plotted is the temporal decay of the horizontal separation distance d_{12} between the rotational centers of the two vortices (1 and 2) in each binary system. The rotational centers are determined as explained in section 2.2 with respect to the vertical average of $\mathbf{u}$ in the nominal boundary layer between $z = 0$ and 1 km (henceforth $\mathbf{u}_{bl}$). The time series for the dry system (dashed black curve) ends when d_{12} drops below the selected terminal value of $d_{12}^t \equiv 3.2\langle r_{mx}\rangle_{12}$. The quantity r_{mx} appearing in the definition of d_{12}^t is the radius where the maximum value of $\bar{v}_{bl}$ (henceforth v_{mx}) occurs in a vortex-centric coordinate system. The angular brackets $\langle \ldots \rangle_{12}$ denote an average of the enclosed variable taken between the two vortices. The preceding choice for d_{12}^t is loosely motivated by studies of nondivergent 2-D vortex merger, where it provides a reasonable approximation for the critical separation distance below which symmetric vorticity cores will rapidly fuse [*Rosso*, 1977; *Saffman and Szeto*, 1980; *Overman and Zabusky*, 1982; *Melander et al*., 1988; *Fine et al*., 1991]. The moist time series (solid red curve) is terminated before d_{12} becomes less than d_{12}^t partly because of vortex tracking difficulties at late times. A brief comparison between the depicted initial deceleration of moist diabatic merger and the aforementioned frictional slowdown of dry merger is deferred until the end of section 5.

One notable event during the evolution of the moist diabatic system is an abrupt contraction of the surface vorticity cores. Figures 14b and 14c illustrate a profound departure of the moist vortices on a frictional ocean from their dry counterparts on a frictionless boundary approximately 45 h into the experiments. At this time, convection induces a sharp acceleration of v_{mx} along with a sharp reduction of r_{mx} in each vortex. A reduction of r_{mx} necessitates closer approach (smaller d_{12}) to trigger the rapid coalescence of vortex cores. It should be remarked that a similar moist simulation with the surface drag coefficient C_d reduced an order of magnitude at $t = 0$ to a constant value of 10^{-4} fails to exhibit a similar contraction event before completion of the merger process.

Although both surface vorticity cores shrink and strengthen in the frictional moist diabatic system, they do so asymmetrically owing to discretization error. The desymmetrization of the moist binary system during core contraction is seen in the attendant drop of $S_v \equiv \min\{v_{mx}\}_{12}/\max\{v_{mx}\}_{12}$, in which $\min\{\ldots\}_{12}$ and $\max\{\ldots\}_{12}$ are the minimum and maximum between vortices 1 and 2 (Figure 14d). While both vortices maintain their integrity for some time after desymmetrization, the final stage of their coalescence is characterized by severe straining of the weaker vortex core [cf., *Melander et al*., 1987; *Dritschel and Waugh*, 1992; *Ritchie and Holland*, 1993; *Prieto et al*., 2003]. Figure 14e (middle right) offers a glimpse of the straining at hour 123 of the simulation.

On another matter, the precipitation pattern of the moist system of surface vortices over a warm ocean (Figure 15) shows some resemblance to that of the midlevel system over a cool ocean (Figure 10a) for several

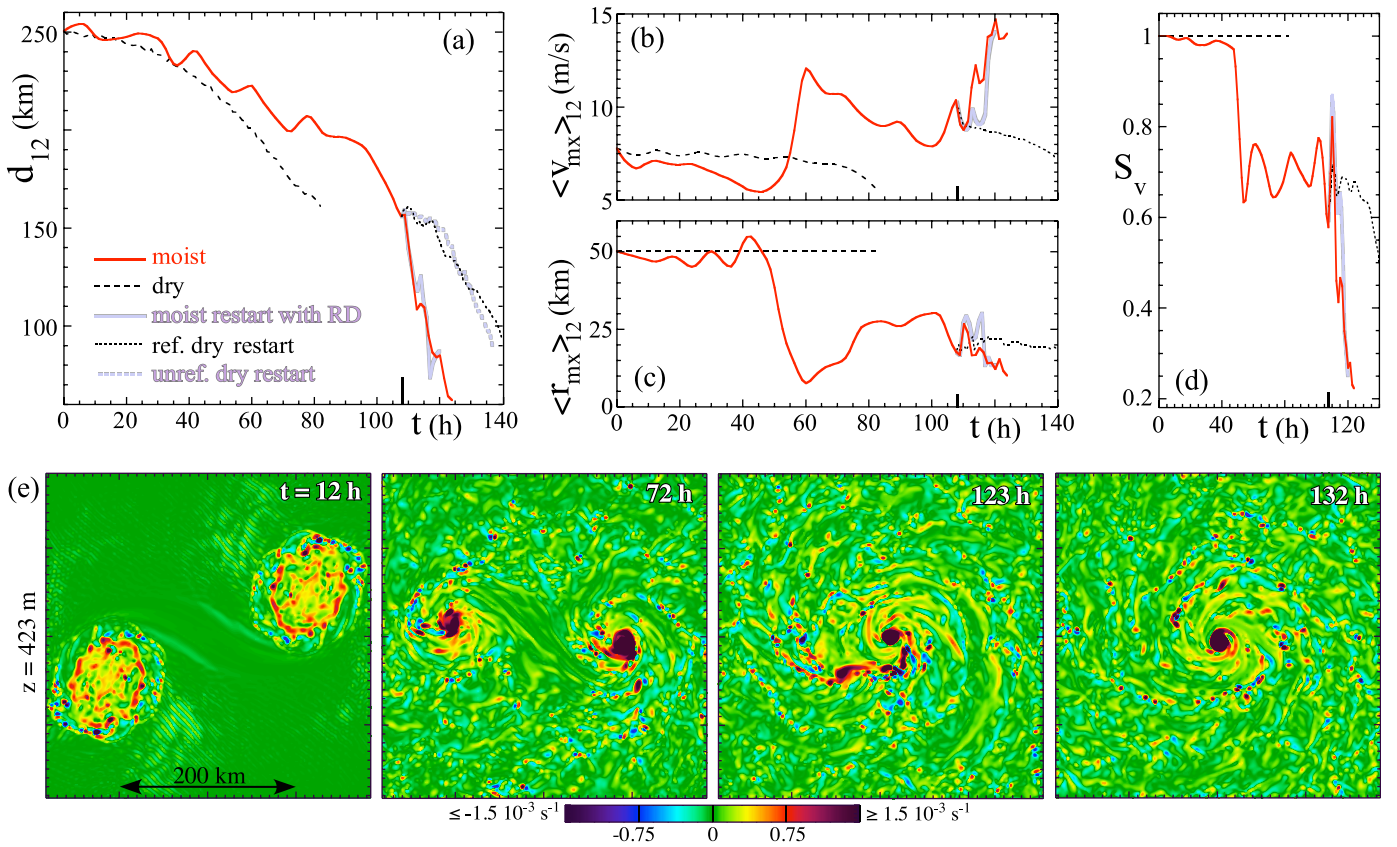

Figure 14. (a)–(d) Selected time series from the moist surface-concentrated binary vortex experiment at high T_s (solid red). Results from the dry adiabatic simulation without surface drag (dashed black) are shown for reference. Also shown are time series of a moist restart (solid light-purple) with severely reduced surface drag (RD), a refined dry restart (dotted black), and an unrefined dry restart (dotted light-purple in Figure 14a). The extended tick mark on the bottom axis of each graph indicates the restart time. (a) The surface-vortex separation distance. (b) The maximum value of vortex-centric $\bar{v}$ (obtained from $\mathbf{u}_{bl}$) averaged between the two surface vortices. (c) The radius of the maximum vortex-centric $\bar{v}$ averaged between the two surface vortices. (d) The velocity based surface-vortex symmetry parameter. The plots in (e) are selected snapshots of the relative vorticity distribution near the surface of the moist system.

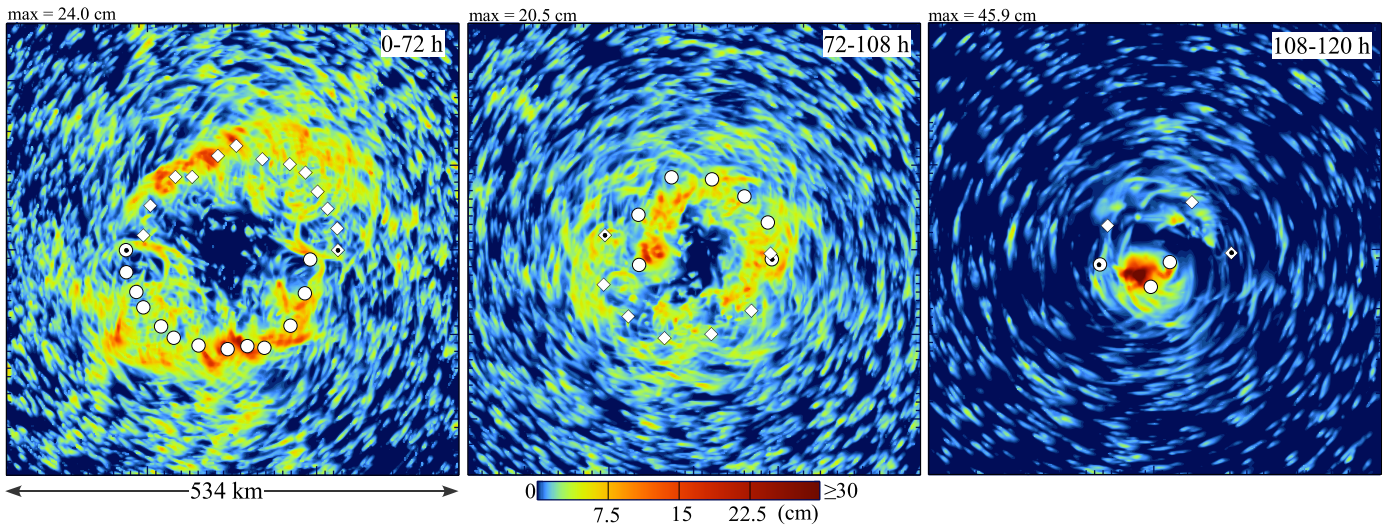

Figure 15. Accumulated rainfall between hours (left) 0–72, (middle) 72–108, and (right) 108–120 of the moist surface-concentrated binary vortex experiment at high T_s. White circles and diamonds show the counterclockwise trajectories of the rotational centers in the boundary layers of each vortex. The rotational centers are plotted every 6 h starting from the symbols with central black dots.

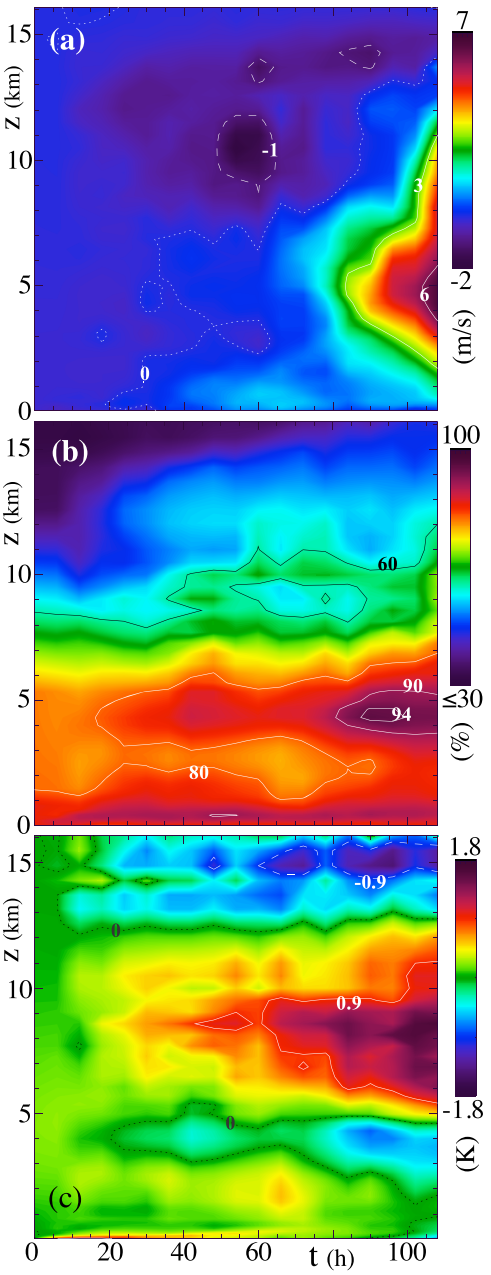

Figure 16. Evolution of (a) system-centric $\bar{v}$ at $\tilde{r}=60$ km, (b) area-averaged RH in the disc defined by $\tilde{r} \leq 60$ km, and (c) area-average of $\theta-\bar{\theta}(\tilde{r}=600\,\text{km}, z, t)$ in the same disc during the first 4.5 days of the experiment on surface-concentrated vortices over a warm ocean. The time axis ends approximately at the onset of accelerated moist surface merger and sharp intensification of the dominant vortex.

days. The rainfall has broader areal extent, but stays concentrated in the vicinity of the vortex trajectories. Subsequently, there is a noticeable shift of the heaviest precipitation radially inward. An especially strong event begins after 108 h of simulation time.

The common perception that moist convection accelerates surface vortex merger appears to become valid by the time of the aforementioned episode of enhanced precipitation. Figure 14a demonstrates that moist surface merger occurs much more rapidly than its counterpart in either of two types of dry restarts (described shortly) initiated 108 h into the experiment. One of the dry restarts (light-purple dotted curve in Figure 14a) incorporates artificial radiation, dissipative heating, surface heat exchange, surface drag, and stratospheric Rayleigh damping. The other (black dotted curve) eliminates all of the aforementioned features from the dynamical equations. The former "unrefined" restart is initialized with no fields modified other than the excluded moisture variables. The latter "refined" restart is initialized in nonlinear balance with both w and $\mathbf{u}_\chi$ set equal to zero; the nondivergent velocity field $\mathbf{u}_\psi$ is slightly altered so as not to vary between $z=0$ and 320 m. The solid light-purple curves in Figures 14a–14d correspond to a moist diabatic restart with the surface drag coefficient severely reduced to a constant value of 10^{-4}. Because these curves do not stray too far from those of the original simulation, the accelerated merger event in the moist diabatic system does not seem to critically depend on the concurrent surface drag over the 12 h comparison period.

A notable occurrence starting before and completing shortly after the restart time is the coalescence of midlevel vortices. Such midlevel merger is a distinguishing feature of the moist experiment, as middle tropospheric vorticity anomalies are irreversibly expelled (displaced radially outward) in the dry adiabatic system initialized at $t=0$. Figure 16 illustrates the time development of selected fields inside or on the perimeter of a circular disc with a radius of 60 km centered at the nonstationary midpoint between the two surface vortices in the moist experiment. The middle-tropospheric growth of $\bar{v}$ on the perimeter of the disc reflects the progression of midlevel merger. The emergence of prominent positive and negative θ-anomalies above and below $z \approx 5$ km inside the disc qualitatively resembles the pattern expected for a system-centered midlevel vortex in a state of approximate thermal-wind balance. The attendant growth of the average middle tropospheric RH (up to 95%) inside the disc appears to be partly attributable to the inward transport of enhanced water vapor content from earlier convection that is trapped within the merging midlevel vortices. One might speculate that greater middle-tropospheric RH inward of the rotational centers of the surface vortices facilitates vigorous deep convection there [*Kilroy and Smith*, 2013; *Davis*, 2015], which in turn could assist surface coalescence.

4.2. Accelerated Merger Dynamics

Figure 17 compares selected time-integrated elements of the $\bar{v}$-budget between hours 110 and 111 of the moist simulation (with standard oceanic surface-drag) to their counterparts in the refined dry restart initiated at $t = 108$ h. The integrals are obtained from data sampled every 4 min. The system-centric coordinate system is defined to have its origin at the time-averaged midpoint between the two surface vortices during the analysis period. The 1 h time-interval under consideration is deemed adequate for illustrating the impact of diabatic processes.

To begin with, the dry $\bar{v}$-budget shows negligible radial influx of absolute vorticity from either the irrotational or nondivergent component of the horizontal flow in the lower troposphere. Similarly, there is negligible redistribution of angular momentum by vertical advection, owing to the zeroing of w upon reinitialization and the removal of cumulus convection from the model. The primary amplification of $\bar{v}$ occurs in the middle troposphere through the negative correlation between u_ψ and η, largely in association with the end-stage of midlevel merger and continued axisymmetrization. By contrast, the moist simulations show significant influx of absolute vorticity in the lower troposphere driven by the irrotational component of the horizontal flow in a radial interval containing the vortex cores. A strong spin-up tendency associated with $-\overline{u_\chi \eta}$ extends into the middle and upper troposphere inward of the mean orbital radius of the surface vortices. This tendency is reinforced by $-\overline{u_\psi \eta}$ but opposed by the vertical advection of angular momentum.

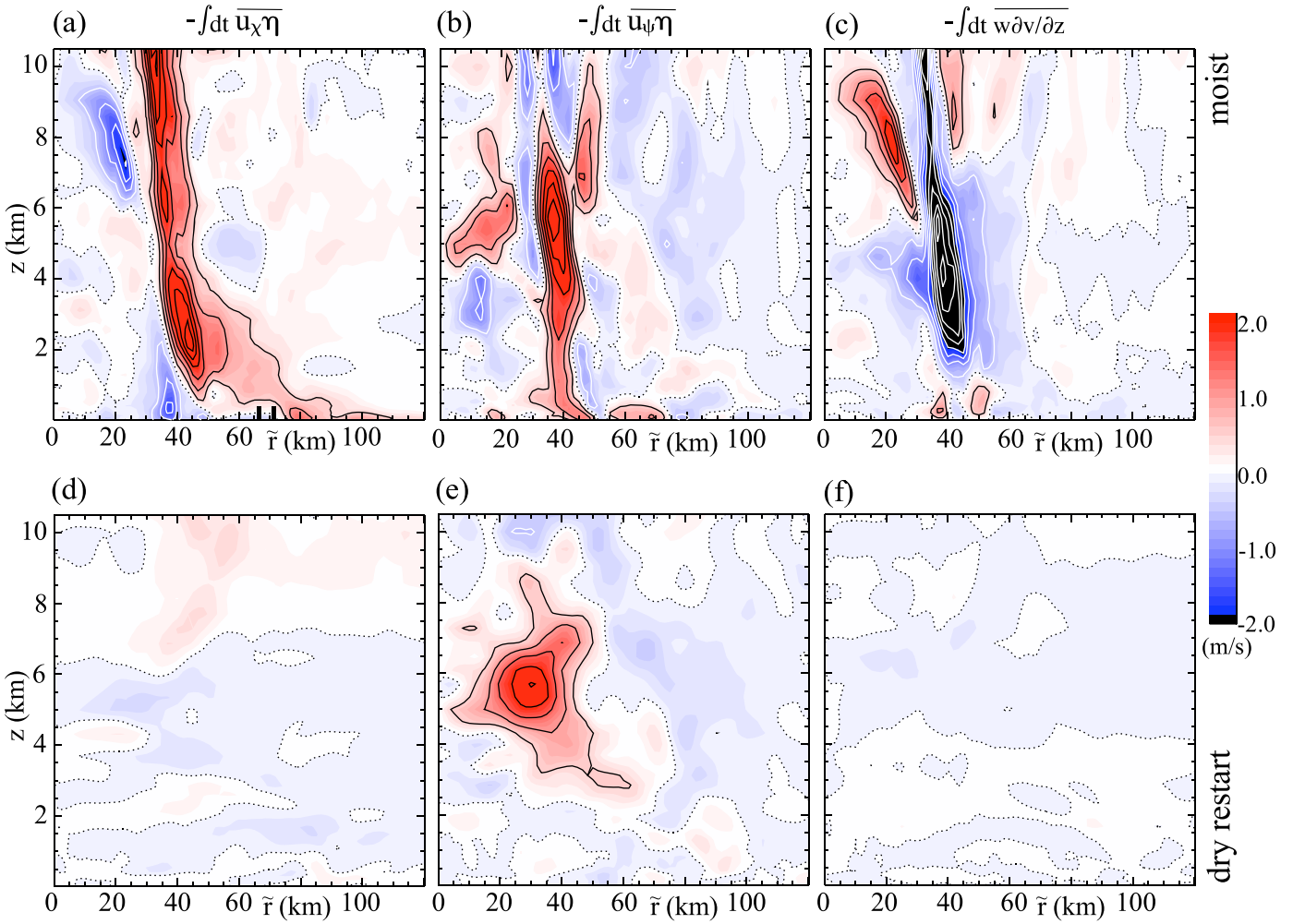

Figure 17. (a)–(c) Selected contributions to the change of system-centric $\bar{v}$ between hours 110 and 111 of the moist binary vortex experiment initialized with surface-concentrated vortices over a warm ocean. (a and b) Time integrals over the 1 h analysis period of the $\bar{v}$-tendencies associated with the radial influx of η driven by (a) the irrotational winds and (b) the nondivergent winds. The extended tick marks at the bottom of (a) indicate the radial coordinates of the surface-vortex centers at the beginning and end of the analysis period; each radial coordinate is an average between the two vortices. (c) Similar time integral of the $\bar{v}$-tendency associated with vertical advection. (d)–(f) As in Figures 17a–c but between hours 2 and 3 of a dry adiabatic restart initialized with the ζ-distribution of the moist experiment at $t = 108$ h. Contours are spaced 0.5 m s^{-1} apart and styled as in Figure 4.

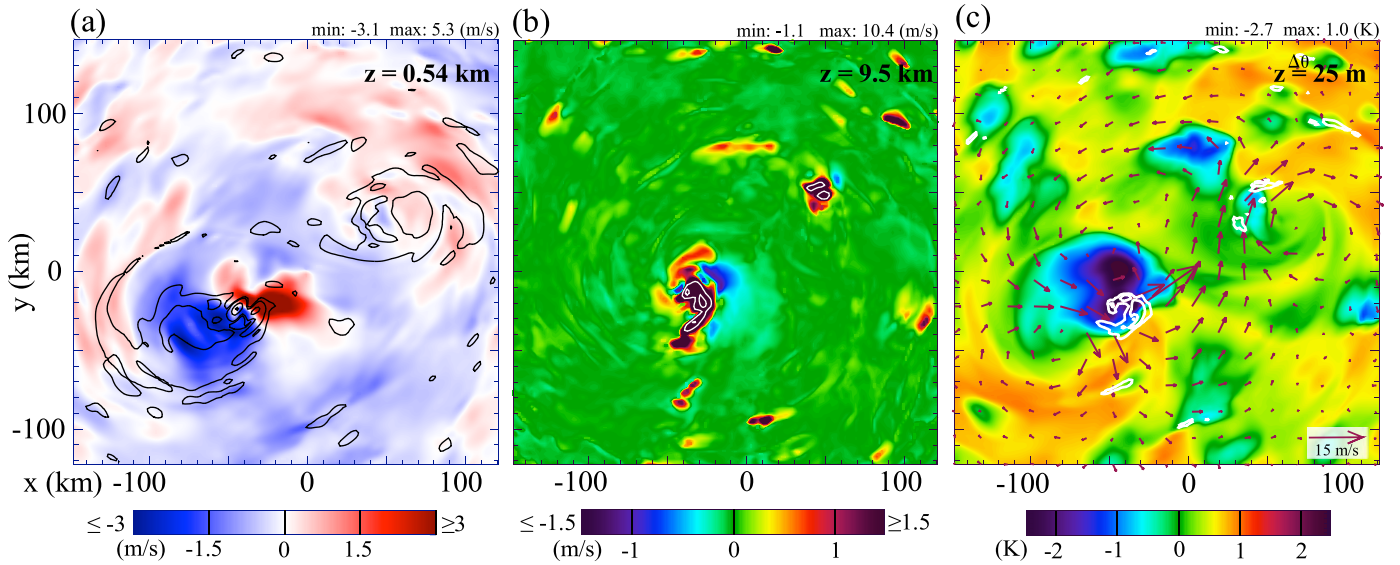

Figure 18. Notable flow features between hours 110 and 111 of the moist binary vortex experiment initialized with surface-concentrated vortices over a warm ocean. (a) The 1 h time averages of the irrotational component of the radial velocity (u_χ, colors) and relative vorticity (ζ, contours) at $z = 0.54$ km. The first/second/third/fourth outermost contour corresponds to 0.025/0.1/0.5/0.9 times the maximal value of ζ. (b) The 1 h time average of vertical velocity w at $z = 9.5$ km. The white contour levels are 3 and 8 m s^{-1}. (c) The 1 h time averages of potential temperature minus its horizontal domain average ($\Delta\theta$, colors) at $z = 25$ m, vertical velocity (w, contours) at $z = 2.1$ km, and the difference in horizontal velocity between $z = 3.1$ and 0.5 km (vectors). The white w-contour levels are 0.5 and 2 m s^{-1}. Note that the shear-vector pattern is similar when the lower level is reduced from 0.5 to 0.15 km (not shown).

Supplemental analysis has verified that the latter opposition is predominantly associated with the updraft component of the vertical advection term, defined by $-\overline{\Theta(w)w\partial v/\partial z}$.

Figure 18a shows relative vorticity contours superimposed on the irrotational component of the radial velocity field near the surface. Both fields are averaged over the 1 h time period chosen above for examination of the $\bar{v}$-budget. There is a prominent couplet of positive and negative u_χ centered at approximately $(x, y) = (-35, -25)$ km. Examination of the vertical velocity distribution indicates that this convergence zone is colocated with a deep convective updraft (Figure 18b) maintained in the approximate down-shear region of a pronounced cold pool (Figure 18c) [cf., *Davis*, 2015]. It is seen that the positive part of the u_χ-couplet is located primarily inward of the lower-left surface vortex, whereas the negative part covers a sizable fraction of the vorticity core. The latter fact suggests that the irrotational component of the horizontal velocity field acts partly to advect the lower-left surface vortex toward its binary companion. As usual, the cumulus updraft also acts to enhance the local relative vorticity [*Montgomery et al.*, 2006; *Kilroy and Smith*, 2013]. Over time, such enhancement appears to have an important role in moving the center of rotation of the lower-left vortex closer to the center of the binary system. Figure 19 illustrates the foregoing process in greater detail over an extended period of analysis. A prominent subvortex is seen to emerge in the region of enhanced convection and rapidly entrain a large portion of the original vorticity core. The entrainment coincides with amplification of v_{mx} (Figure 14b) and motion of the rotational center radially inward. Enhanced convection in the vicinity of the dominant vortex persists with some variability as the surface merger event progresses. In time, the dominant vortex consumes its weaker companion and evolves into an intense hurricane.

5. Discussion

The eventual diabatic acceleration of merger in the surface-concentrated system (section 4.2) agrees with conventional wisdom, but stands in contrast to the analyzed behavior of the midlevel system over a cooler ocean (section 3.2). The conflicting results are found in association with distinctions in the basic characteristics of moist convection during the events under consideration. During the first episode of midlevel merger, artificial radiation and cloud processes interfered with the dry adiabatic, baroclinic merger mechanism without introducing a faster pathway to vortex coalescence. The failure of moisture to expedite merger coincided with minimal initiation of deep convection inward of the orbital radius of the binary system (Figure

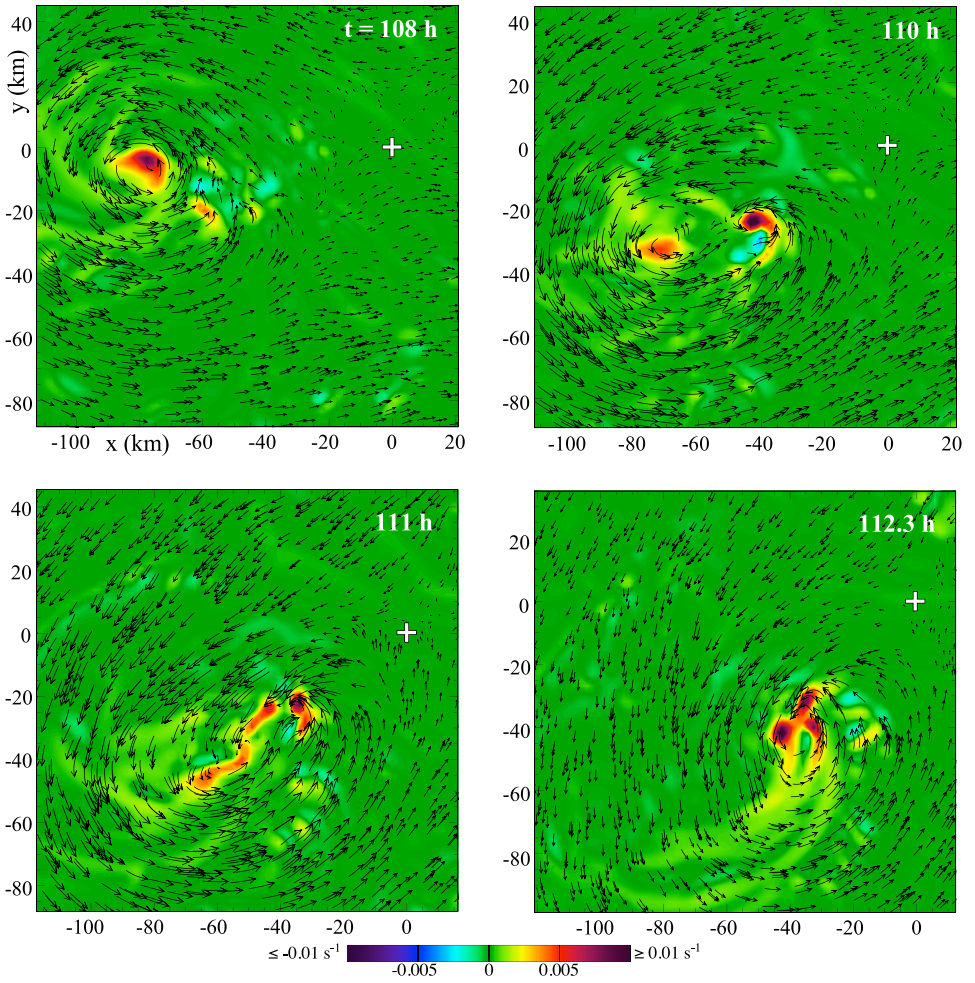

Figure 19. Complex evolution of the stronger vortex during the early phase of diabatically accelerated approach toward its binary companion, starting 4.5 days into the experiment initialized with surface-concentrated vortices over a warm ocean. Each plot shows instantaneous horizontal streamlines (black) superimposed on relative vorticity (color) at $z = 0.54$ km. The length of each streamline segment is proportional to the local wind speed, but the scaling varies between plots. The displayed domain is fixed relative to earth, but the coordinates on each axis slightly change with time so that the origin remains at the midpoint between the two vortices of the binary system (white plus-sign). Such instantaneous midpoints are distinct from the 1 h time-average that defines the origin in Figure 18. The time of each snapshot is shown on the upper right corner of the corresponding plot. Note that the pronounced vorticity anomaly at $(x, y) \approx (-42, -24)$ km in the upper right plot ($t = 110$ h) traces back to the weaker anomaly at approximately $(-58, -20)$ km in the upper left plot ($t = 108$ h).

10). By contrast, accelerated surface merger over a warmer ocean distinctly involved a period of strong deep convection on the inward edge of the core of a particular vortex (Figure 18). The second episode of midlevel merger resembled a nondivergent 2-D process with minimal diabatic acceleration. Further examination of the event (not shown) revealed deep convection occurring both inward and outward of the merging vortices. Of seemingly greater importance toward limiting diabatic effects over the merger period, the convective activity was relatively weak in a manner explained below.

One reasonable measure of convective intensity is the central vertical mass-flux. The central vertical mass-flux at height z is presently taken to be the areal average of ρw within a radius of 125 km from the center of the binary system. The density ρ in the preceding definition is that of moist air, excluding hydrometeors. Figure 20a compares the central vertical mass-flux profiles during two of the merger events under consideration. The solid curve in the right graph shows the temporal mean of the profile during the accelerated merger of surface-concentrated vortices over a warm ocean. The dashed and dotted curves convey the temporal variability of the mass-flux over the analysis period, as explained in the caption. The left graph is similar to the right graph, but for the first 12 h of the second episode of vortex merger in the midlevel

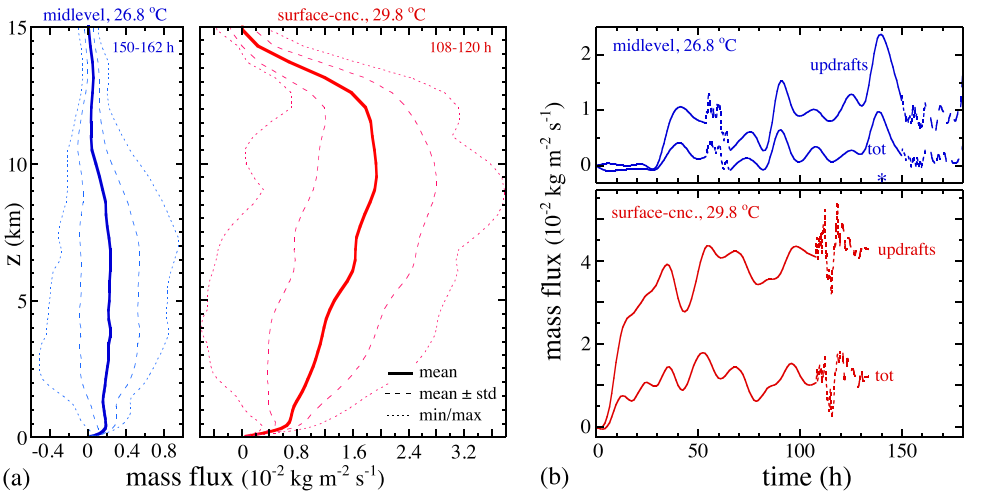

Figure 20. (a) Areal-averaged vertical mass-flux (ρw) within a 125 km radius of the system center in the moist experiments initialized with (left) midlevel vortices over a cool ocean and (right) surface-concentrated vortices over a warm ocean. Solid curves correspond to temporal means over the 12 h analysis periods printed at the top of each graph. Dashed curves correspond to the mean ± 1 standard deviation. Dotted curves correspond to the minimum and maximum areal-averaged mass-fluxes observed during the analysis period. The extrema at different values of z need not have occurred at the same time. (b) Time series of the areal-averaged vertical mass-flux within a 175 km radius of the system center and the contribution from updrafts alone at $z = 9$ km for (top) the midlevel system over a cool ocean and (bottom) the surface-concentrated system over a warm ocean. The total areal average (tot) is the sum of the aforementioned positive updraft component M_+ and a negative downdraft component M_-, in which $M_\pm \equiv \int_A d^2\mathbf{x}\rho w\Theta(\pm w)/A$ and A is the area of the averaging disc. The solid/long-dashed/dashed segments of each curve are obtained from data archived every 6/1/0.067 h. The asterisk on the bottom axis of the top graph roughly indicates where convective processes generate the vortices involved in the second episode of midlevel merger over a cool ocean.

system over a cooler ocean (cf., Figures 13a–13f). Despite the occurrence of moderately strong updrafts during this time frame, the mean vertical mass-flux is relatively small. Furthermore, there is minimal vertical gradient in the middle-tropospheric merger layer, indicating little mean radial inflow at the periphery of the system. The time series in Figure 20b verify that the vertical mass-flux in the upper troposphere of the midlevel system is practically always less than its counterpart in the surface-concentrated system over a warmer ocean. Here, the spatial averaging disc has been expanded to a radius of 175 km to cover areas of dense precipitation during the early stages of each experiment.

One might wonder whether raising the sea-surface temperature (T_s) under middle tropospheric vortices would accelerate their coalescence, or whether lowering the sea-surface temperature would slow the merger of surface-concentrated vortices. Definitive answers may well require large ensemble studies owing to the possibility of significant stochastic variability of cloud-scale convection. Nevertheless, two additional experiments have been conducted for the purpose of gaining some preliminary insight. Synopses of each experiment are given below.

Raising T_s from 26.8 to 29.8 °C in the midlevel system predictably amplifies the mean surface-flux of moist enthalpy and the mean CAPE of air in the boundary layer in the broad vicinity of each vortex. Deep convection becomes vigorous earlier in the simulation and maintains greater intensity during the merger process. Convective intensity here refers to either the total vertical mass-flux or the contribution from updrafts alone, measured 9 km above sea-level in any disc with an outer radius $\tilde{r}$ of 125–200 km. Although appreciable precipitation appears to be broader in radial coverage (as in Figure 15), the greatest rainfall accumulations are consistently generated within or nearby each vortex. The mutual approach of midlevel vorticity cores again suffers diabatic slowdown for several days. During the same period, the average surface wind speed within (say) 200 km of the center of the binary system grows faster than its counterpart over the cooler ocean. Moreover, shortly after 3 days of simulation time, the maximum φ-averaged tangential velocity at the surface of each vortex rapidly intensifies beyond middle tropospheric values (6–9 m s^{-1}) to approximately 12 m s^{-1}. The intensification event leaves the system asymmetric. Subsequent surface spin-up further desymmetrizes the binary system in that only one of the two vortices continues to strengthen in the boundary layer. The stronger vortex entrains its weaker companion over the next 2–3 days. Middle tropospheric entrainment occurs first (in less than 2 days) and resembles the asymmetric merger process of a dry

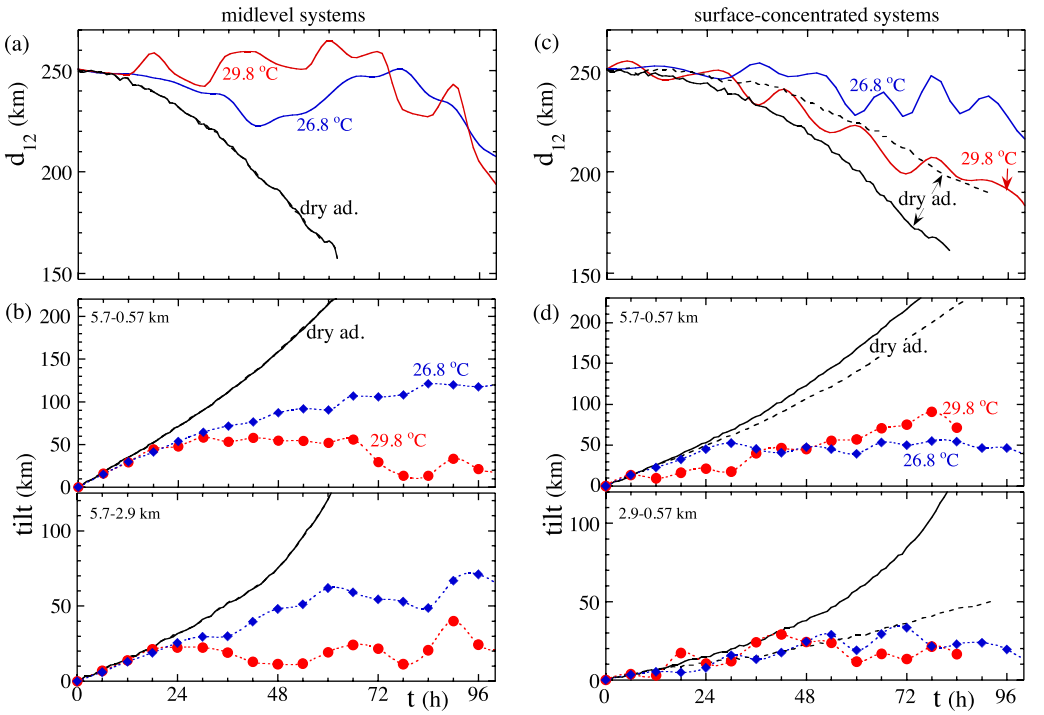

Figure 21. Initial slowdown of merger and the attendant reduction of misalignments. (a) Time series of the vortex separation distance d_{12} in several midlevel systems. The separation distance corresponds to that between rotational centers in a thin layer of the middle troposphere centered at $z = 5.7$ km. Here and in (b)-(d), the blue curve is for a moist diabatic system with surface fluxes activated and T_s=26.8°C. The red curve is for a similar system with T_s=29.8°C. The black curves are for dry adiabatic systems with (dashed) and without (solid) surface drag. (b) Time series of the average vertical misalignment (tilt) of the two vortices in each binary system in Figure 21a. The top graph shows the average horizontal distance between rotational centers in the middle tropospheric layer (z=5.7±0.4 km) and boundary layer ($z \leq 1.1$ km) of a vortex. The bottom graph shows the average horizontal distance between rotational centers in the middle tropospheric layer and a selected lower tropospheric layer (z=2.9±0.3 km). Note that the solid and dashed black curves in Figures 21a and 21b very closely overlap and are virtually indistinguishable. (c and d) As in Figures 21a and 21b but for simulations initialized with surface-concentrated vortices. The separation distance d_{12} in Figure 21c is obtained from rotational centers in the boundary layer. The tilts in Figure 21d are measured between (top) the middle tropospheric and boundary layers, or (bottom) the lower tropospheric and boundary layers. The numbers on the top-left corners of each graph in Figures 21b and 21d are the central heights of the upper and lower layers used to measure the tilts.

adiabatic restart initialized 12 h after the rapid intensification event. The same restart fails to reproduce surface coalescence with or without surface drag for at least 6 days. Eventually, the prevailing vortex transitions into a severe hurricane.

In summary, there are two main consequences of raising the sea-surface temperature under a midlevel system. First, increasing T_s causes the vortices to become surface-dominant prior to coalescence. Second, increasing T_s in an imperfect numerical simulation desymmetrizes the binary system and the merger process. Nevertheless, the approximate 5 day time frame for the coalescence of middle tropospheric vorticity cores does not appreciably change. Of further note, the diabatic acceleration of surface merger seen in relation to the dry restart is consistent with the experiment initialized with surface-concentrated vortices over a warm ocean.

Lowering T_s from 29.8 to 26.8 °C in the surface-concentrated system of section 4 decreases the average surface-flux of moist enthalpy and lessens the growth of the mean CAPE of air in the boundary layer. Deep convection requires more time to intensify and remains weaker in the disc-averaged sense throughout the merger process. As before, the greatest rainfall accumulations are generated within or nearby each vortex. The diabatic surface vortices take nearly 10 days to merge, compared to approximately 5.5 days for the moist system over a warm ocean and 3.5 days for a dry adiabatic surface system with a free-slip bottom boundary condition. The maximum tangential wind speed of each surface vortex decays to approximately 5 m s^{-1}, reintensifies to 11–12 m s^{-1} over the interval $80 < t < 130$ h, and subsequently decays toward its earlier minimum before merger completes. The final day of surface merger, which begins after midlevel

vorticity coalescence, proceeds moderately faster than the same phase of merger in a dry adiabatic restart with or without surface drag. After the process completes, the system readily transforms into a tropical cyclone. In short, the main consequences of lowering the sea-surface temperature under a surface-concentrated system are the tempering of vortex intensification and the delay of coalescence.

One notable outcome of three in four of the diabatic experiments under consideration is the clear initial slowdown of meso-β scale vortex coalescence. Figure 21 verifies that slowdown invariably occurs in association with a reduction of the vertical misalignments that are theoretically required for the principal dry adiabatic merger mechanism to operate. The surface-concentrated vortices over a warm ocean appear to exhibit a relatively small deceleration of mutual approach, despite maintaining limited misalignment. In fact, there is no deceleration relative to the merger of surface-concentrated vortices in a dry adiabatic system on a frictional boundary. Frictional slowdown of merger in the dry adiabatic surface system coincides with reduction of vertical misalignment in the lower troposphere (Figure 21d) and partial spin-down of each vortex. The diabatic surface system over a warm ocean exhibits a deeper reduction of misalignment (Figure 21d) and an episode of pronounced spin-up (Figure 14b). While these changes and other flow modifications introduced by diabatic processes may be important individually, they are seen to have minimal net effect on the initial merger rate.

6. Conclusions

This study has examined the coalescence of meso-β scale cyclonic vortices in idealized numerical experiments with potential relevance to oceanic tropical weather systems. The main objective was to advance current understanding of how diabatic processes modify or essentially change the prevailing mechanism of vortex merger that is found in a dry adiabatic system. The preceding objective was achieved by directly comparing moist diabatic and dry adiabatic simulations. The former simulations included two-moment cloud microphysics, artificial radiation, and a basic parameterization of air-sea interaction. Analysis of the simulation output focused on the phase of vortex merger that occurs before the rapid fusion of vorticity cores.

Starting from either baroclinic state depicted in Figure 2, the dry merger process resembled that expounded by *Schecter* [2016]. The aforementioned paper provisionally concluded that the relevant merger mechanism relies on the natural rotations of vortex misalignments that are induced by the mutual shearing of the constituent vortices of the binary system. Such rotations can result in merger by swinging the leading section of each vertically sheared vortex radially inward, as the trailing sections of weaker intensity swing outward. Here it was shown that the irrotational winds are theoretically important to the natural rotation of a misalignment in the parameter regime under consideration. It was therefore reasonable to find that the irrotational winds played a leading role in driving the influx of absolute vorticity in the dry merger experiments.

The incorporation of diabatic features into the cloud model usually changed the picture of vortex coalescence. Analysis focused on a midlevel system over a cool ocean and a surface-concentrated system over a warm ocean. For the midlevel problem at low T_s, artificial radiation considerably slowed merger, and moist convection failed to expedite the process. Evidence suggested that both artificial radiation and moist convection hindered the development of vortex misalignments that seem to be necessary for the dry adiabatic merger mechanism to operate. The diabatic slowdown of vortex merger does not appear to be a statistical anomaly. Similar slowdowns were observed during the initial stages of merger in a midlevel system at high T_s and a surface-concentrated system at low T_s.

Serendipitously, the moist midlevel system over a cool ocean spawned a second pair of meso-β scale vortices after the original pair had merged. The behavior of the new binary system resembled that of a 2-D nondivergent barotropic system in which the vorticity cores are driven together as a result of their interaction with background vorticity. The preceding result suggests that ideal 2-D hydrodynamics should not always be dismissed as irrelevant for explaining the prerapid fusion phase of meso-β scale vortex merger in a moist convective system. In principle, applicability requires a 2-D dynamical time scale no greater than the time scales of competing baroclinic or diabatic merger mechanisms.

For the surface-concentrated problem considered over a warmer ocean, diabatic cloud processes generated stronger convection and had distinct consequences. In conjunction with surface friction, moist convection induced a dramatic contraction and moderate desymmetrization of the surface vortices roughly midway into the experiment. The subsequent merger of the surface vortices lagged the coalescence of vorticity in the middle troposphere. Following a build-up of midlevel vorticity and relative humidity inward of the surface vortices, their merger continued much faster than in dry restarts with or without surface fluxes, dissipative heating, and artificial radiation. The pronounced acceleration of merger was evidently driven by deep cumulus convection that arose on the inward edge of one of the two surface vorticity cores. The rotational center of this particular core rapidly moved toward the focal point of the convection, and thereby moved closer to the center of the binary system. The inward migration occurred simultaneously with vortex intensification. The intensification continued, and the vortex eventually entrained its weaker companion. Although details may differ from case to case, an eventual stage of diabatically accelerated surface merger appears to be fairly common. Such an effect was also found in experiments initialized with midlevel vortices over a warm ocean and surface-concentrated vortices over a cool ocean.

Admittedly, there remains much more to be learned about the fundamental dynamics of mesoscale vortex coalescence. As in the present study, some unexpected results will likely emerge from future numerical experiments having different configurations. The challenge will be not merely to elucidate the variety of vortex coalescence mechanisms and their domains of applicability, but also to elucidate the impact of the merger process on tropical cyclone development. As seen in *Schecter* [2016], the impact is not necessarily positive.

Appendix A: The Helmholtz Decomposition

The analysis software used for this study finds $\mathbf{u}_\chi \equiv \nabla_h\chi$ and $\mathbf{u}_\psi \equiv \hat{z}\times\nabla_h\psi$ in the area of interest through an approach that is independent of the particular model boundary conditions. In this approach, the divergence and vorticity fields (σ and ζ) are set to zero outside of a circular disc whose radius $\tilde{r}_b$ is far beyond the vortex interaction region. The Poisson equations (7) for χ and ψ with the aforementioned truncated sources are solved as though the system were in an unbounded domain. The third component of the velocity field in the circular disc is given by $\mathbf{u}_\vartheta = \nabla_h\vartheta$, in which $\nabla_h^2\vartheta = 0$ subject to $\partial\vartheta/\partial\tilde{r} = u - u_\chi - u_\psi$ at $\tilde{r}_b$.

To elaborate, at each vertical level, $\mathbf{u}$ is interpolated onto a polar grid with 1024 (356) azimuthal (radial) increments. The azimuthal increments are uniform, whereas the radial increments match those of the CM1 grid along the x (or y) axis starting from the center. The maximum polar grid radius is $\tilde{r}_b^+ \approx 1720$ km, in which $\tilde{r}_b^+$ modestly exceeds $\tilde{r}_b$. Following interpolation, vorticity and divergence are calculated on the polar grid. A discretized version of the azimuthal Fourier transform (FT) of the vector Poisson equation,

$$\left[\frac{d^2}{d\tilde{r}^2} + \frac{1}{\tilde{r}}\frac{d}{d\tilde{r}} - \frac{n^2}{\tilde{r}^2}\right]\begin{pmatrix}\chi_n\\ \psi_n\end{pmatrix} = \begin{pmatrix}\sigma_n\\ \zeta_n\end{pmatrix}\Theta(\tilde{r}_b - \tilde{r}), \tag{A1}$$

is then solved for the FTs of χ and ψ. The boundary conditions satisfied at $\tilde{r} = 0$ are $(\chi_n, \psi_n) = 0$ for $|n| \geq 1$ and $d(\chi_0, \psi_0)/d\tilde{r} = 0$. The boundary conditions imposed at $\tilde{r}_b^+$ are $d(\chi_n, \psi_n)/d\tilde{r} = -n(\chi_n, \psi_n)/\tilde{r}$ for $|n| \geq 1$ and $d(\chi_0, \psi_0)/d\tilde{r} = (\chi_0, \psi_0)/\tilde{r}\ln(\tilde{r})$. The preceding conditions are obtained from analytical free-space solutions that are physically acceptable as $\tilde{r} \to \infty$. A similar procedure is used to find ϑ_n, but with the right-hand side of the analogue of equation (A1) set to zero and the outer boundary condition given by $d\vartheta_n/d\tilde{r} = u_n - u_{\chi,n} - u_{\psi,n}$ at $\tilde{r}_b$ on a slightly smaller grid. The FTs of the radial and azimuthal components of $\mathbf{u}_{\chi/\psi/\vartheta}$ are obtained directly from $\chi_n/\psi_n/\vartheta_n$ and readily inverted.

For all cases considered in the main text, it has been verified that differences between $-\overline{u\eta}$ and $-(\overline{u_\chi\eta} + \overline{u_\psi\eta})$ are negligibly small, owing to the condition $|\mathbf{u}_\vartheta| \ll |\mathbf{u}|$ in the region of concern.

Appendix B: Technical Notes on Misalignment Modes

B1. Structure and Computation of an Asymmetric Normal Mode

Consider an isolated vortex possessing a barotropic basic state in gradient and hydrostatic balance. Let (r, φ, z) denote a stationary vortex-centric cylindrical coordinate system, with z corresponding to the pressure-based pseudo-height of *Hoskins and Bretherton* [1972]. Suppose that perturbations (marked with primes) to the basic

state variables (marked with overbars and dependent only on radius) are governed by the linearized hydrostatic primitive equations with a Boussinesq approximation, subject to the boundary conditions $w = 0$ at $z = 0$ and $2H$. Note that here and throughout this appendix, w represents the vertical pseudovelocity. Modal and quasi-modal solutions to the aforementioned perturbation equations are discussed in *Schecter and Montgomery* [2004 (SM04)] and *Menelaou et al.* [2016 (M16)].

It is readily shown that the normal modes of the vortex are perturbations of the form

$$[u', v', \phi'] = a[U(r), V(r), \Phi(r)]e^{i(n\varphi-\omega t)}\cos\left(\frac{m\pi z}{2H}\right) + c.c., \tag{B1a}$$

$$w' = aW(r)e^{i(n\varphi-\omega t)}\sin\left(\frac{m\pi z}{2H}\right) + c.c., \tag{B1b}$$

in which ϕ' is the geopotential perturbation, $a \equiv |a|e^{i\varphi_a}$ is a complex mode amplitude, and $c.c.$ denotes the complex conjugate of the term to the left. Hereafter, it is assumed that $n \geq 1$. The geopotential wave function Φ satisfies a second-order homogeneous ordinary differential equation in r that parametrically depends on ω (equation (39) of SM04 or equation (18) of M16 with $H \to 2H$). Acceptable values of ω are those allowing Φ to be noninfinite at the origin while also satisfying a specific radiation or evanescence condition (depending on the value of ω) as r tends toward infinity. The outer asymptotic condition used for the present study will be discussed shortly.

Relevant to the forthcoming discussion, it can be shown that

$$U = \frac{i}{\bar{\eta}\bar{\xi} - v^2}\left[v\frac{d\Phi}{dr} - \frac{n\bar{\xi}}{r}\Phi\right] \tag{B2a}$$

$$V = \frac{1}{\bar{\eta}\bar{\xi} - v^2}\left[\bar{\eta}\frac{d\Phi}{dr} - \frac{nv}{r}\Phi\right], \tag{B2b}$$

in which $\bar{\eta} \equiv r^{-1}d(r^2\bar{\Omega})/dr + f$, $\bar{\xi} \equiv 2\bar{\Omega} + f$, and $v \equiv \omega - n\bar{\Omega}$ [SM04]. It can also be shown that $\Phi \sim r^n$ as $r \to 0$ [SM04]. Taking into consideration that $\bar{\eta} \to \bar{\xi}$ in the same limit, equations (B2a) and (B2b) imply that $V \sim iU$ as $r \to 0$. Letting φ_u (φ_v) denote the phase of U (V), it follows that

$$\varphi_v - \varphi_u \to \pi/2 \tag{B3}$$

as r becomes infinitesimally small.

The Helmholtz partitioning of the horizontal velocity field associated with a vortex perturbation that rapidly decays as r tends to infinity in an unbounded domain is written as follows:

$$\begin{pmatrix} u' \\ v' \end{pmatrix} = \begin{pmatrix} \dfrac{\partial\chi'}{\partial r} - \dfrac{1}{r}\dfrac{\partial\psi'}{\partial\varphi} \\ \dfrac{1}{r}\dfrac{\partial\chi'}{\partial\varphi} + \dfrac{\partial\psi'}{\partial r} \end{pmatrix}. \tag{B4}$$

For modal perturbations, the velocity potential χ' and the stream function ψ' have the form $(\chi', \psi') = a[\mathcal{X}(r), \Psi(r)]e^{i(n\varphi-\omega t)}\cos(m\pi z/2H) + c.c.$ From equations (B1a) and (B4), it follows that

$$U = U_\chi + U_\psi \quad \text{and} \quad V = V_\chi + V_\psi, \tag{B5a}$$

in which

$$\begin{pmatrix} U_\chi \\ V_\chi \end{pmatrix} \equiv \begin{pmatrix} \dfrac{d\mathcal{X}}{dr} \\ \dfrac{in}{r}\mathcal{X} \end{pmatrix} \quad \text{and} \quad \begin{pmatrix} U_\psi \\ V_\psi \end{pmatrix} \equiv \begin{pmatrix} -\dfrac{in}{r}\Psi \\ \dfrac{d\Psi}{dr} \end{pmatrix}. \tag{B5b}$$

The wave functions $\mathcal{X}$ and Ψ satisfy a transformed vector Poisson equation similar to equation (A1); specifically,

$$\left[\frac{d^2}{dr^2} + \frac{1}{r}\frac{d}{dr} - \frac{n^2}{r^2}\right]\begin{pmatrix} \mathcal{X} \\ \Psi \end{pmatrix} = \begin{pmatrix} D \\ Z \end{pmatrix}, \tag{B6}$$

in which $D(r) \equiv [d(rU)/dr + inV]/r$ is the divergence wave function and $Z(r) \equiv [d(rV)/dr - inU]/r$ is the vorticity wave function. Equation (B6) can be solved with a Green function method subject to the conditions that $\mathcal{X}$ and Ψ do not become infinite as $r \to 0$ or ∞. Substituting the solution into equation (B5b) yields

$$\begin{bmatrix} U_\chi(r) \\ V_\chi(r) \end{bmatrix} = \int_0^\infty dr' r' D(r') \begin{bmatrix} \frac{\partial}{\partial r} G_n(r,r') \\ \frac{in}{r} G_n(r,r') \end{bmatrix} \text{ and } \begin{bmatrix} U_\psi(r) \\ V_\psi(r) \end{bmatrix} = \int_0^\infty dr' r' Z(r') \begin{bmatrix} -\frac{in}{r} G_n(r,r') \\ \frac{\partial}{\partial r} G_n(r,r') \end{bmatrix}, \tag{B7}$$

in which the Green function is given by

$$G_n(r,r') \equiv -\frac{1}{2n}\left(\frac{r_<}{r_>}\right)^n \quad n \geq 1. \tag{B8}$$

The symbol $r_<$ ($r_>$) is used here to denote the lesser (greater) of r and r'.

The neutral misalignment mode discussed near the end of section 3.1.2 of the main text belongs to a meso-β scale cyclone whose basic-state vorticity is given by

$$\bar{\zeta} = \frac{\zeta_o}{1 + (r/r_c)^{40}}, \tag{B9}$$

in which the value of the constant ζ_o yields $\bar{v} = 5.3$ m s^{-1} at $r_c = 50$ km. The frequency and geopotential wave function were found using a shooting method nearly identical to that described in SM04 and M16. One caveat is that the frequency of the mode was too small to permit inertia-gravity wave radiation ($\omega < f$). The large-r solution of the wave function used to determine the outer radial boundary condition was therefore modified to have a nonoscillatory, exponentially decaying controlling factor. Specifically, the outer boundary condition was changed to $d\Phi/dr = -\left[1 - (\omega/f)^2\right]^{1/2} \Phi/l_R$, in which $l_R \equiv N(2H)/m\pi f$ is the internal Rossby deformation radius. The mode found by the shooting method agreed well with that dominating the simulated linear response of the vortex to a finite period of misalignment forcing. The linear model providing the aforementioned result was that of *Schecter* [2015], with the vertical wavelength of the forcing function equated to that of the mode at issue.

Figure A1 depicts the vorticity and divergence wave functions of the computed misalignment mode. Although the divergence wave function is two orders of magnitude smaller than the vorticity wave function, it is an order of magnitude wider. Moreover, section 3.1.2 provides evidence that the irrotational velocity perturbation associated with the divergence wave function has an important influence on the slow rotation of the misalignment.

B2. Orbital Motion of A Potential Vorticity Centroid

The Lagrangian equations of motion for the cylindrical coordinates (r_p, φ_p, z_p) of a fluid parcel in a vortex possessing a barotropic basic-state can be written

$$\frac{dr_p}{dt} = u'(r_p, \varphi_p, z_p, t), \tag{B10a}$$

$$\frac{d\varphi_p}{dt} = \bar{\Omega}(r_p) + v'(r_p, \varphi_p, z_p, t)/r_p, \tag{B10b}$$

$$\frac{dz_p}{dt} = w'(r_p, \varphi_p, z_p, t). \tag{B10c}$$

Suppose that the vortex is perturbed with a single misalignment mode (equations (B1a) and (B1b)) having $n = 1$ and $m = 2$. The particular mode under consideration is assumed to be neutral, such that ω is real.

One can readily verify that the uniform circular orbit given by

$$\begin{aligned} r_p &= 2\left|\frac{aU_0 \cos\left(\pi z_{pi}/H\right)}{\omega - \bar{\Omega}_0}\right| \\ \varphi_p &= \omega t - \varphi_a - \varphi_{u0} - (2j+1)\pi/2 \end{aligned} \tag{B11}$$

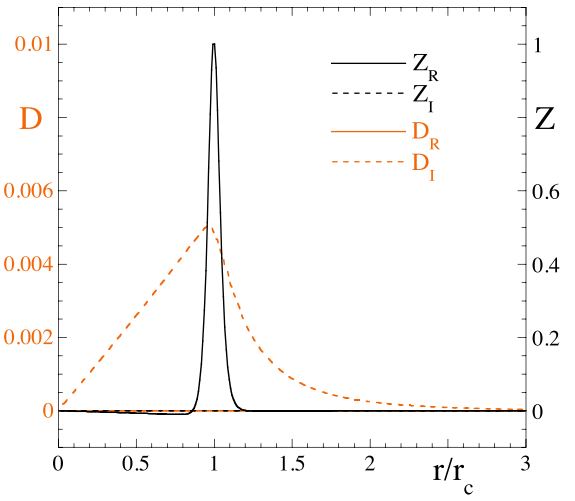

Figure A1. Wave functions for the vorticity ($Z \equiv Z_R + iZ_I$) and divergence ($D \equiv D_R + iD_I$) of the misalignment mode, normalized to the peak value of Z_R.

is a valid solution of equations (B10a) and (B10b) upon neglecting corrections that are higher order in the small mode amplitude $|a|$. In the preceding equations, z_{pi} is the initial value of z_p, j is an integer satisfying $\cos(j\pi) = \mathrm{sgn}\left[\cos(\pi z_{pi}/H)/(\omega - \bar{\Omega}_0)\right]$, and all variables with zero subscripts are evaluated at $r = 0$. Verification of the bottom equation requires the small-r asymptotic relation $V \sim iU$ derived in Appendix B1.

It is now informally demonstrated that the parcel trajectory given by equation (B11) is that of the PV centroid. Assume that the inner part of the misalignment mode consists of small, shape-preserving lateral displacements of the basic-state PV distribution ($\bar{q}$) that vary with both z and t. Over the bulk of such a disturbance,

$$q' = -\frac{d\bar{q}}{dr} r_* \cos(\varphi - \varphi_*), \tag{B12a}$$

in which q' is the PV perturbation, and $[r_*(z,t), \varphi_*(z,t)]$ is the polar coordinate vector of the PV centroid that is displaced from the origin nonuniformly in z. Based on the linearized PV equation [SM04; M16],

$$\left[\frac{\partial}{\partial t} + \bar{\Omega}\frac{\partial}{\partial \varphi}\right] q' = -u'\frac{d\bar{q}}{dr},$$

it is also provable that the modal PV perturbation can be written

$$q' = -\frac{d\bar{q}}{dr}\frac{2|a||U|}{\omega - \bar{\Omega}} \cos(\varphi - \omega t + \varphi_a + \varphi_u + \pi/2) \cos\left(\frac{\pi z}{H}\right). \tag{B12b}$$

Equating the right-hand sides of (B12a) and (B12b) yields

$$r_* = \frac{2|a||U|}{\omega - \bar{\Omega}} \frac{\cos(\varphi - \omega t + \varphi_a + \varphi_u + \pi/2)}{\cos(\varphi - \varphi_*)} \cos\left(\frac{\pi z}{H}\right). \tag{B13a}$$

For r_* to be consistently independent of φ requires that

$$\varphi_* = \omega t - \varphi_a - \varphi_u - (2j+1)\pi/2, \tag{B13b}$$

in which j is an integer chosen to ensure positivity of r_*. The latter condition is satisfied if $\cos(j\pi) = \mathrm{sgn}\left[\cos(\pi z/H)/(\omega - \bar{\Omega})\right]$. In keeping with our focus on a perturbation near the center of the vortex ($r \lesssim |a|^{\gamma} r_c$, $0 < \gamma < 1$), the variables $|U|$, φ_u and $\bar{\Omega}$ can be evaluated at $r = 0$ in equations (B13a) and (B13b) with negligible error. It follows that r_* and φ_* are equivalent to r_p and φ_p given by equation (B11).

B3. Helmholtz Decomposition of the Centroid's Orbital Angular Velocity

The angular velocity of a generic fluid parcel in a perturbed vortex is readily decomposed into contributions from $\bar{\Omega}$, v'_χ/r_p and v'_ψ/r_p (equation (11), top line). If the perturbation consists solely of the $(m,n) = (2,1)$ misalignment mode, one may write

$$\frac{d\varphi_p}{dt} = \bar{\Omega}(r_p) + \frac{2|a|}{r_p} \Re\left\{\left[V_\chi(r_p) + V_\psi(r_p)\right] e^{i(\varphi_p - \omega t + \varphi_a)}\right\} \cos\left(\frac{\pi z_p}{H}\right), \tag{B14}$$

in which V_χ and V_ψ are obtained from equation (B7). For the fluid parcel which carries the PV centroid, r_p and φ_p given by equation (B11) are substituted into the denominator and exponential of the second term on the right-hand side of equation (B14). In addition, r_p is set to zero in the arguments of $\bar{\Omega}$ and $V_{\chi/\psi}$. The errors introduced by the preceding approximations vanish as $|a|$ tends toward zero. With the final

substitutions $|U_0| \rightarrow |V_0|$ and $\varphi_{u0} \rightarrow \varphi_{v0} - \pi/2$ (cf., Appendix B1), equation (B14) becomes the bottom line of equation (11) with $\omega_{\chi/\psi}$ given by equation (12).

Acknowledgments
This work was supported by NSF grant AGS-1250533. The author thanks David Nolan and anonymous referees for their constructive comments during the review process. The author also thanks George Bryan of the National Center for Atmospheric Research (NCAR) for providing the cloud model (CM1) that was used for the numerical experiments. The computational resources required to conduct the simulations were provided by NCAR/CISL through allocation UNWR0002. The simulation data files are currently available from the author upon request at schecter@nwra.com.

References

Bishop, C. H. (1996), Domain-independent attribution. Part I: Reconstructing the wind from estimates of vorticity and divergence using free space Green's functions, *J. Atmos. Sci.*, *53*, 241–252.
Bretherton, C. S., P. N. Blossey, and M. Khairoutdinov (2005), An energy-balance analysis of deep convective self-aggregation above uniform SST, *J. Atmos. Sci.*, *62*, 4273–4292.
Bryan, G. H., and J. M. Fritsch (2002), A benchmark simulation for moist nonhydrostatic numerical models, *Mon. Wea. Rev.*, *130*, 2917–2928.
Carnevale, G. F., P. Cavazza, P. Orlandi, and R. Purini (1991), An explanation for anomalous vortex merger in rotating-tank experiments, *Phys. Fluids A*, *3*, 1411–1415.
Chang, S. W. (1983), A numerical study of the interactions between two tropical cyclones, *Mon. Weather Rev.*, *111*, 1806–1817.
Davis, C. A. (2015), The formation of moist vortices and tropical cyclones in idealized simulations, *J. Atmos. Sci.*, *72*, 3499–3516.
Davis, C. A., and D. A. Ahijevych (2013), Thermodynamic environments of deep convection in Atlantic tropical disturbances, *J. Atmos. Sci.*, *70*, 1912–1928.
DeMaria, M., and J. C. Chan (1984), Comments on "A numerical study of the interactions between two tropical cyclones," *Mon. Weather Rev.*, *112*, 1643–1645.
Donelan, M. A., B. K. Haus, N. Reul, W. J. Plant, M. Stiassnie, H. C. Graber, O. B. Brown, and E. S. Saltzman (2004), On the limiting aerodynamic roughness of the ocean in very strong winds, *Geophys. Res. Lett.*, *31*, L18306, doi:10.1029/2004GL019460.
Drennan, W. M., J. A. Zhang, J. R. French, C. McCormick, and P. G. Black (2007), Turbulent fluxes in the hurricane boundary layer: Part II: Latent heat flux, *J. Atmos. Sci.*, *64*, 1103–1115.
Dritschel, D. G., and D. W. Waugh (1992), Quantification of the inelastic interaction of unequal vortices in two-dimensional vortex dynamics, *Phys. Fluids A*, *4*, 1737–1744.
Dunion, J. P. (2011), Rewriting the climatology of the tropical North Atlantic and Caribbean Sea atmosphere, *J. Clim.*, *24*, 893–908.
Dunkerton, T. J., M. T. Montgomery, and Z. Wang (2009), Tropical cyclogenesis in a tropical wave critical layer: Easterly waves, *Atmos. Chem. Phys.*, *9*, 5587–5646.
Fairall, C. W., E. F. Bradley, J. E. Hare, A. A. Grachev, and J. B. Edson (2003), Bulk parameterization of air-sea fluxes: Updates and verification for the COARE algorithm, *J. Clim.*, *16*, 571–591.
Falkovich, A. I., A. P. Khain, and I. Ginis (1995), Motion and evolution of binary tropical cyclones in a coupled atmosphere-ocean numerical model, *Mon. Weather Rev.*, *123*, 1345-–1363.
Fang, J., and F. Zhang (2011), Evolution of multiscale vortices in the development of Hurricane Dolly (2008), *J. Atmos. Sci.*, *68*, 103–122.
Fine, K. S., C. F. Driscoll, J. H. Malmberg, and T. B. Mitchell (1991), Measurements of symmetric vortex merger, *Phys. Rev. Lett.*, *67*, 588–591.
Hendricks, E. A., M. T. Montgomery, and C. A. Davis (2004), The role of "vortical" hot towers in the formation of Tropical Cyclone Diana, *J. Atmos. Sci.*, *61*, 1209–1232.
Hoskins, B. J., and F. P. Bretherton (1972), Atmospheric frontogenesis models: Mathematical formulation and solution, *J. Atmos. Sci.*, *29*, 11–37.
Houze, R. A., W. C. Lee, and M. M. Bell (2009), Convective contribution to the genesis of hurricane Ophelia (2005), *Mon. Weather Rev.*, *137*, 2778–2800.
Jones, S. C. (1995), The evolution of vortices in vertical shear. I: Initially barotropic vortices, *Q. J. R. Meteorol. Soc.*, *121*, 821–851.
Khain, A., I. Ginis, A. Falkovich, and M. Frumin (2000), Interaction of binary tropical cyclones in a coupled tropical cyclone-ocean model, *J. Geophys. Res.*, *105*, 22,337–22,354.
Kieu, C. Q., and D.-L. Zhang (2010), Genesis of tropical storm Eugene (2005) from merging vortices associated with ITCZ breakdowns. Part III: Sensitivity to various genesis parameters, *J. Atmos. Sci.*, *67*, 1745–1758.
Kilroy, G., and R. K. Smith (2013), A numerical study of rotating convection during tropical cyclogenesis, *Q. J. R. Meteorol. Soc.*, *139*, 1255–1269.
Melander, M. V., N. J. Zabusky, and J. C. McWilliams (1987), Asymmetric vortex merger in two dimensions: Which vortex is victorious?, *Phys. Fluids*, *30*, 2610–2612.
Melander, M. V., N. J. Zabusky, and J. C. McWilliams (1988), Symmetric vortex merger in two dimensions: Causes and conditions, *J. Fluid Mech.*, *195*, 303–340.
Menelaou, K., D. A. Schecter, and M. K. Yau (2016), On the relative contribution of inertia-gravity wave radiation to asymmetric instabilities in tropical cyclone-like vortices, *J. Atmos. Sci.*, *73*, 3345–3370.
Montgomery, M. T., M. E. Nicholls, T. A. Cram, and A. B. Saunders (2006), A vortical hot tower route to tropical cyclogenesis, *J. Atmos. Sci.*, *63*, 355–386.
Morrison, H., J. A. Curry, and V. I. Khvorostyanov (2005), A new double-moment microphysics parameterization for application in cloud and climate models. Part I: Description, *J. Atmos. Sci.*, *62*, 1665–1677.
Morrison, H., G. Thompson, and V. Tatarskii (2009), Impact of cloud microphysics on the development of trailing stratiform precipitation in a simulated squall line: Comparison of one-and two-moment schemes, *Mon. Weather Rev.*, *137*, 991–1007.
Nolan, D. S. (2007), What is the trigger for tropical cyclogenesis?, *Aust. Meteorol. Mag.*, *56*, 241–266.
Overman, E. A., and N. J. Zabusky (1982), Evolution and merger of isolated vortex structures, *Phys. Fluids*, *25*, 1297–1305.
Prieto, R., B. D. McNoldy, S. R. Fulton, and W. H. Schubert (2003), A classification of binary tropical cyclone-like vortex interactions, *Mon. Weather Rev.*, *131*, 2656–2666.
Reasor, P. D., and M. T. Montgomery (2015), Evaluation of a heuristic model for tropical cyclone resilience, *J. Atmos. Sci.*, *72*, 1765–1782.
Reasor, P. D., M. T. Montgomery, and L. D. Grasso (2004), A new look at the problem of tropical cyclones in shear flow: Vortex resiliency, *J. Atmos. Sci.*, *61*, 3–22.
Reasor, P. D., M. T. Montgomery, and L. F. Bosart (2005), Mesoscale observations of the genesis of Hurricane Dolly (1996), *J. Atmos. Sci.*, *62*, 3151–3171.
Renfrew, I. A., A. J. Thorpe, and C. H. Bishop (1997), The role of the environmental flow in the development of secondary frontal cyclones, *Q. J. R. Meteorol. Soc.*, *123*, 1653–1675.
Ritchie, E. A., and G. J. Holland (1993), On the interaction of tropical-cyclone-scale vortices. II. Discrete vortex patches, *Q. J. R. Meteorol. Soc.*, *119*, 1363–1379.

Ritchie, E. A., and G. J. Holland (1997), Scale interactions during the formation of Typhoon Irving, *Mon. Weather Rev.*, *125*, 1377–1396.
Rosso, V. J. (1977), Convective merging of vortex cores in lift generated wakes, *J. Aircraft*, *14*, 283–290.
Rotunno, R., and K. A. Emanuel (1987), An air-sea interaction theory for tropical cyclones: Part II. Evolutionary study using a nonhydrostatic axisymmetric numerical model, *J. Atmos. Sci.*, *44*, 542–561.
Saffman, P. G., and R. Szeto (1980), Equilibrium shapes of a pair of equal uniform vortices, *Phys. Fluids*, *23*, 2339–2342.
Schecter, D. A. (2011), Evaluation of a reduced model for investigating hurricane formation from turbulence, *Q. J. R. Meteorol. Soc.*, *137*, 155–178.
Schecter, D. A. (2015), Response of a simulated hurricane to misalignment forcing compared to predictions of a simple theory, *J. Atmos. Sci.*, *72*, 1235–1260.
Schecter, D. A. (2016), Development and nondevelopment of binary mesoscale vortices into tropical cyclones in idealized numerical experiments, *J. Atmos. Sci.*, *73*, 1223–1254.
Schecter, D. A., and M. T. Montgomery (2004), Damping and pumping of a vortex Rossby wave in a monotonic cyclone: Critical layer stirring versus inertia-buoyancy wave emission, *Phys. Fluids*, *16*, 1334–1348.
Schecter, D. A., D. H. E. Dubin, K. S. Fine, and C. F. Driscoll (1999), Vortex crystals from 2D Euler flow: Experiment and simulation", *Phys. Fluids*, *11*, 905–914.
Simpson, J., E. Ritchie, G. J. Holland, J. Halverson, and S. Stewart (1997), Mesoscale interactions in tropical cyclone genesis, *J. Atmos. Sci.*, *125*, 2643–2661.
Sippel, J. A., J. Nielsen-Gammon, and S. E. Allen (2006), The multiple-vortex nature of tropical cyclogenesis, *Mon. Weather Rev.*, *134*, 1796–1814.
Smith, R. K., and M. T. Montgomery (2012), Observations of the convective environment in developing and non-developing tropical disturbances, *Q. J. R. Meteorol. Soc.*, *138*, 1721–1739.
Soga, Y., Y. Kiwamoto, A. Sanpei, and J. Aoki (2003), Merger and binary structure formation of two discrete vortices in a background vorticity distribution of a pure electron plasma, *Phys. Plasmas*, *10*, 3922–3926.
Tory, K. J., M. T. Montgomery, N. E. Davidson, and J. D. Kepert (2006), Prediction and diagnosis of tropical cyclone formation in an NWP system. Part II: A diagnosis of Tropical Cyclone Chris formation, *J. Atmos. Sci.*, *63*, 3091–3113.
Verron, J., and S. Valcke (1994), Scale-dependent merging of baroclinic vortices, *J. Fluid Mech.*, *264*, 81–106.
Von Hardenberg, J., J. C. McWilliams, A. Provenzale, A. Shchepetkin, and J. B. Weiss (2000), Vortex merging in quasi-geostrophic flows, *J. Fluid Mech.*, *412*, 331–353.
Wang, Y., and G. J. Holland (1995), On the interaction of tropical-cyclone-scale vortices. IV: Baroclinic vortices, *Q. J. R. Meteorol. Soc.*, *121*, 95–126.
Wang, Y., and G. J. Holland (1996), Tropical cyclone motion and evolution in vertical shear, *J. Atmos. Sci.*, *53*, 3313–3332.
Zhang, D. L., and C. Q. Kieu (2006), Potential vorticity diagnostics of a simulated hurricane. Part II: Quasi-balanced contributions to forced secondary circulations, *J. Atmos. Sci.*, *63*, 2898–2914.